Hydraulic tomography in fractured granite: Mizunami Underground Research site, Japan

Walter A. Illman,[1] Xiaoyi Liu,[2] Shinji Takeuchi,[3] Tian-Chyi Jim Yeh,[4] Kenichi Ando,[5] and Hiromitsu Saegusa[3]

Received 29 November 2007; revised 17 September 2008; accepted 10 October 2008; published 8 January 2009.

[1] Two large-scale cross-hole pumping tests were conducted at depths of 191–226 m and 662–706 m in deep boreholes at the Mizunami Underground Research Laboratory (MIU) construction site in central Japan. During these two tests, induced groundwater responses were monitored at many observation intervals at various depths in different boreholes at the site. We analyze the two cross-hole pumping tests using transient hydraulic tomography (THT) based on an efficient sequential successive linear estimator to compute the hydraulic conductivity (K) and specific storage (S_s) tomograms, as well as their uncertainties in three dimensions. The equivalent K and S_s estimates obtained using asymptotic analysis treating the medium to be homogeneous served as the mean parameter estimates for the 3-D stochastic inverse modeling effort. Results show several, distinct, high K and low S_s zones that are continuous over hundreds of meters, which appear to delineate fault zones and their connectivity. The THT analysis of the tests also identified a low K zone which corresponds with a known fault zone trending NNW and has been found to compartmentalize groundwater flow at the site. These results corroborate well with observed water level records, available fault information, and coseismic groundwater level responses during several large earthquakes. The successful application of THT to cross-hole pumping tests conducted in fractured granite at this site suggests that THT is a promising approach to delineate large-scale K and S_s heterogeneities, fracture connectivity, and to quantify uncertainty of the estimated fields.

Citation: Illman, W. A., X. Liu, S. Takeuchi, T.-C. J. Yeh, K. Ando, and H. Saegusa (2009), Hydraulic tomography in fractured granite: Mizunami Underground Research site, Japan, *Water Resour. Res.*, *45*, W01406, doi:10.1029/2007WR006715.

1. Introduction

[2] The accurate prediction of fluid flow and radionuclide transport in the subsurface is critical in the design of high-level nuclear waste repositories. Geologic formations of low hydraulic conductivity (K) of igneous origins (e.g., crystalline rocks such as granite, basalt, tuffs, etc.) have been suggested as suitable sites for the construction of nuclear waste repositories in many countries. These geologic formations, however, often contain interconnected fractures or fault zones on a continuum of scales [*Bonnet et al.*, 2001] caused by cooling and/or tectonic processes. These fractures strongly affect groundwater flow and contaminant transport, as flow is predominantly carried through a limited number of major fractures. Therefore, the accurate characterization of the limited number of large fractures and fault zones, as well as their connectivity is of paramount importance in predicting the hydraulic behavior around a nuclear waste repository.

[3] To quantitatively comprehend, describe, and predict flow and solute transport processes in fractured geologic media, a mathematical model is essential. Comprehensive reviews of mathematical models of flow and transport in fractured geologic media can be found in paper by *Neuman* [1987], *Bear et al.* [1993], *National Research Council* (*NRC*) [1996], *Illman et al.* [1998], *Berkowitz* [2002], *MacQuarrie and Mayer* [2005], and *Neuman* [2005].

[4] A fractured geologic medium is a mixture of two or more distinct populations of voids (i.e., fractures of various sizes and the matrix pore space). In general, fractures are highly elongated voids (open conduits), which are generally sparsely distributed in geologic media. The matrix pore space of geologic media, on the other hand, is an aggregation of a large number of small granular voids. Over the past few decades, many mathematical models have emerged on the basis of different conceptualizations of fractured geologic media. For example, our inability to characterize these two void populations in detail and the consideration of practicality led to the creation of the equivalent porous media concept [e.g., *Bear*, 1972; *Peters and Klavetter*, 1988; *Dykhuizen*, 1990; *Pruess et al.*, 1990]. Effects of the contrast of the two void populations and the slow mixing process between fractures and the matrix then necessitated the use of dual porosity/mass transfer model

[1]Department of Earth and Environmental Sciences, University of Waterloo, Waterloo, Ontario, Canada.
[2]Department of Civil and Environmental Engineering, Stanford University, Stanford, California, USA.
[3]Japan Atomic Energy Agency, Mizunami, Japan.
[4]Department of Hydrology and Water Resources, University of Arizona, Tucson, Arizona, USA.
[5]Civil Engineering Technology Division, Obayashi Corporation, Tokyo, Japan.

0043-1397/09/2007WR006715$09.00

[e.g., *Bibby*, 1981; *Moench*, 1984; *Zimmerman et al.*, 1993; *McKenna et al.*, 2001; *Reimus et al.*, 2003]. In the dual porosity model, the fracture continuum acts to conduct and store fluids, while the matrix only stores fluids. A dual permeability model [*Duguid and Lee*, 1977; *Gerke and van Genuchten*, 1993a, 1993b; *Wu et al.*, 2002; *Illman and Hughson*, 2005] is used when both the fracture and matrix continua conduct and store fluids. These models are, however, only suitable for describing or predicting the flow and transport behavior averaged over a large volume of fractured media, which often fail to meet our high-resolution requirements with respect to contaminant transport investigations. The desire for high-resolution predictions, thus promoted the development of discrete fracture network models [e.g., *Long et al.*, 1982; *Schwartz et al.*, 1983; *Smith and Schwartz*, 1984; *Andersson and Dverstorp*, 1987; *Dershowitz and Einstein*, 1988; *Dverstorp and Andersson*, 1989; *Cacas et al.*, 1990a, 1990b; *Dverstrop et al.*, 1992; *Slough et al.*, 1999; *Park et al.*, 2001a, 2001b, 2003; *Darcel et al.*, 2003; *Benke and Painter*, 2003; *Cvetkovic et al.*, 2004; *Painter and Cvetkovic*, 2005; *Wellman and Poeter*, 2005].

[5] The discrete fracture approach, however, demands detailed specification of fracture geometries and spatial distributions. Uncertainty in characterizing fractures due to our limited characterization technologies then becomes the logic behind the stochastic continuum concept [*Neuman*, 1987; *Tsang et al.*, 1996; *Di Federico and Neuman*, 1998a, 1998b; *Di Federico et al.*, 1999; *Hyun et al.*, 2002; *Ando et al.*, 2003; *Molz et al.*, 2004; *Illman and Hughson*, 2005].

[6] On the basis of these models, different techniques for fractured rock characterization have evolved over the past few decades. For example, *Hsieh et al.* [1985] conducted cross-hole hydraulic tests to obtain the anisotropy of K by treating the fractured rock to be an equivalent homogeneous medium. *Illman and Neuman* [2000, 2001, 2003] and *Illman and Tartakovsky* [2005a, 2005b] studied airflow in unsaturated fractured tuffs and fracture connectivity through cross-hole pneumatic injection tests. *Vesselinov et al.* [2001a, 2001b] used a numerical inverse model to analyze cross-hole pneumatic injection tests conducted by *Illman* [1999; see also *Illman et al.*, 1998] and showed that the delineation of subsurface heterogeneity in both permeability and porosity is possible through pneumatic tomography. Several other researchers [*Guimerà et al.*, 1995; *Hsieh*, 1998; *Marechal et al.*, 2004; *Martinez-Landa and Carrera*, 2005; *Illman and Tartakovsky*, 2006] interpreted various hydraulic tests conducted at different scales in fractured crystalline rocks, while other researchers utilized cross-hole flowmeter tests to characterize fractured rocks [e.g., *Williams and Paillet*, 2002; *Le Borgne et al.*, 2006]. According to *Williams and Paillet* [2002] and *Le Borgne et al.* [2006], cross-hole flowmeter pulse tests define subsurface connections between discrete fractured intervals through short periods of pumping and the corresponding monitoring of pressure pulse propagation using a flowmeter.

[7] In an attempt to further the characterization approaches of fractured rocks and their connectivity, *Day-Lewis et al.* [2000] developed an approach which uses simulated annealing to condition geostatistical simulations of high K zones in fractured rock to hydraulic connection data from multiple cross-hole tests. Their approach yielded valuable insights into the 3-D geometry of fracture zones at the USGS Fractured Rock Hydrology Research Site (i.e., Mirror Lake site) in New Hampshire, USA, but was based on binary classification of K and single cutoff on connectivity. Another limitation of their approach was that hydraulic data was not considered during simulated annealing. This required generation of a large number of realizations to find those that simulate head data well. Despite these limitations, *Day-Lewis et al.* [2000] made significant advances in incorporating hydraulic connectivity information into their groundwater model.

[8] In a different study at the Mirror Lake facility, *Day-Lewis et al.* [2003] demonstrated a strategy to identify preferential flow paths in fractured rocks by combining geophysical data and conventional hydraulic tests. In particular, these authors utilized cross-well difference attenuation ground-penetrating radar to monitor saline-tracer migration at the Mirror Lake site in New Hampshire. *Day-Lewis et al.* [2006] further conducted an integrated interpretation of field experimental cross-hole radar, tracer, and hydraulic data at a fractured rock aquifer at the same site and found that combining time-lapse geophysical monitoring with conventional hydrologic measurements improved the characterization of a fractured-rock aquifer.

[9] The concept of connectivity including its meaning as well as measurement techniques and modeling approaches are still under considerable debate [e.g., *Knudby and Carrera*, 2005, 2006; *Neuman*, 2005; *Illman*, 2004, 2005, 2006]. Many of the aforementioned studies, nonetheless, highlight the importance of connectivity of fractures and other geologic features. In terms of flow, the presence of well-connected fractured rocks could mean significant groundwater resources. In terms of groundwater quality, connectivity of fractures can determine the extent of groundwater contamination. In addition, fracture connectivity also plays an important role on our scientific understanding of flow and transport in fractured rocks. For example, *Illman* [2004] compared permeability estimates obtained from single-hole pneumatic injection tests conducted at various scales (0.5, 1, 2, 3, and 20-m scales) in single boreholes at the Apache Leap Research Site (ALRS) in central Arizona, USA and discovered that the permeability (k) scale effect previously observed by others [*Illman et al.*, 1998; *Illman and Neuman*, 2001, 2003; *Vesselinov et al.*, 2001b; *Hyun et al.*, 2002] was suppressed. At the ALRS, the k scale effect was previously observed through the comparison of k estimates from single-hole and cross-hole tests. *Illman* [2004] reasoned that suppression of k scale effect within a single borehole was due to limited fracture connectivity near the injection interval during single-hole tests.

[10] *Illman* [2006] then showed a strong evidence of a k scale effect through the steady state interpretation of cross-hole pneumatic injection tests alone (i.e., without the comparison of cross-hole k estimates to those from single-hole tests). He reasoned that a more credible evidence for a k scale effect can be obtained from a single test type instead of comparing k estimates from various measurement techniques (i.e., core versus slug versus single-hole versus cross-hole tests). The other new discovery was the concept of directional k scale effect in which the k increases in certain directions but not in others. These observations led *Illman* [2006] to hypothesize that the k scale effect is controlled by the connectivity of fluid conducting fractures, which also

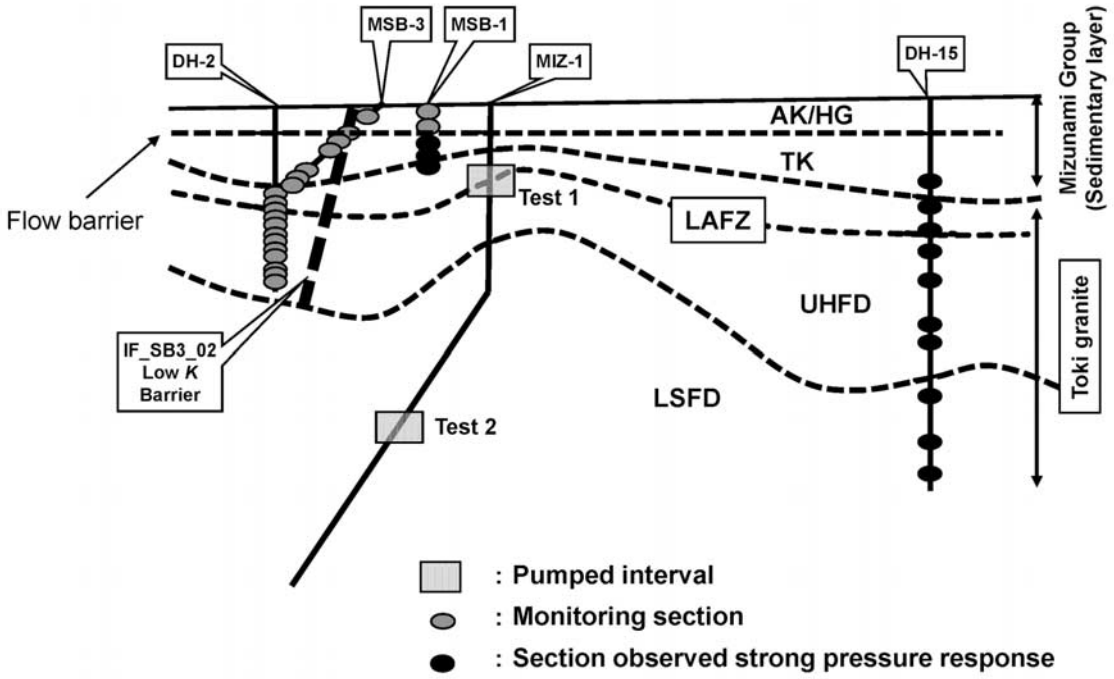

Figure 1. Conceptual diagram showing the boreholes, the pumped and observation intervals as well as the local geology (after S. Takeuchi et al., unpublished data, 2007). The dashed curves approximately delineate contact among various geologic units.

increases with scale, but its connectivity varies directionally. He further reasoned that his hypothesis is consistent with existing scaling theories in fracture connectivity [*Bour and Davy*, 1998; *Darcel et al.*, 2003], although subsurface fracture connectivity in three dimensions could not be measured directly with presently available techniques without destroying the geologic medium. *Illman* [2006] then concluded that the estimation of connectivity of flowing fractures should be possible through hydraulic and pneumatic tomography (HT and PT, respectively) [e.g., *Gottlieb and Dietrich*, 1995; *Butler et al.*, 1999; *Vasco et al.*, 2000; *Yeh and Liu*, 2000; *Vesselinov et al.*, 2001a, 2001b; *Bohling et al.*, 2002; *Hendricks Franssen and Gómez-Hernández*, 2002; *Brauchler et al.*, 2003; *McDermott et al.*, 2003; *Zhu and Yeh*, 2005, 2006; *Illman et al.*, 2007, 2008; *Liu et al.*, 2007; *Li et al.*, 2007, 2008].

[11] Promising results showing the effectiveness of HT have been recently published. For example, using sandbox experiments and an HT analysis algorithm (sequential successive linear estimator, sequential successive linear estimator (SSLE) by *Yeh and Liu* [2000], *Liu et al.* [2002] demonstrated that steady state HT (SSHT) is an effective technique for depicting the K heterogeneity with only a limited number of invasive observations. While HT remains to be fully assessed in the field, there are some additional encouraging results from recent sandbox experiments [*Illman et al.*, 2007, 2008; *Liu et al.*, 2007]. In particular, *Liu et al.* [2007] recently demonstrated that not only did transient HT (THT) identify the pattern of the K heterogeneity, but also the variation of S_s values in the sandbox. More interestingly, the estimated fields from THT successfully predicted the observed drawdown as a function of time of an independent aquifer test [*Liu et al.*, 2007].

[12] In the field, a recent application of THT to a well field at Montalto Uffugo Scalo, Italy produced an estimated transmissivity field that is deemed consistent with the geology of the site [*Straface et al.*, 2007]. Likewise, a HT based on steady shape analysis [*Bohling et al.*, 2002] was tested in the field by *Bohling et al.* [2007]. *Hao et al.* [2008] recently applied HT to a synthetically generated fractured rock and found that HT is effective in imaging the fractures zones, connectivities and their uncertainties if multiple pumping tests and observation data are available. HT thus appears to be a potentially viable high-resolution aquifer and fractured media characterization technology.

[13] The main objective of this paper is to apply the developed THT data analysis algorithm of *Zhu and Yeh* [2005] to two cross-hole pumping tests conducted at the Mizunami Underground Research Laboratory (MIU) construction site in central Japan to demonstrate the potential utility of the HT survey concept as well as the algorithm for characterizing fracture distribution, connectivity, their hydraulic parameters (K and S_s) and corresponding uncertainty estimates. Success of this application, may promote the use of hydraulic and other types of tomographic surveys (e.g., pneumatic and tracer) for mapping fractures and their connectivities as well as their uncertainties in both saturated and unsaturated geologic media.

2. Site Description

2.1. Site Location Description

[14] The Mizunami Underground Research Laboratory (MIU) is located in Mizunami, in the central part of the main island (Honshu) of Japan. The site has been operated by the Japan Atomic Energy Agency (JAEA) since 2002.

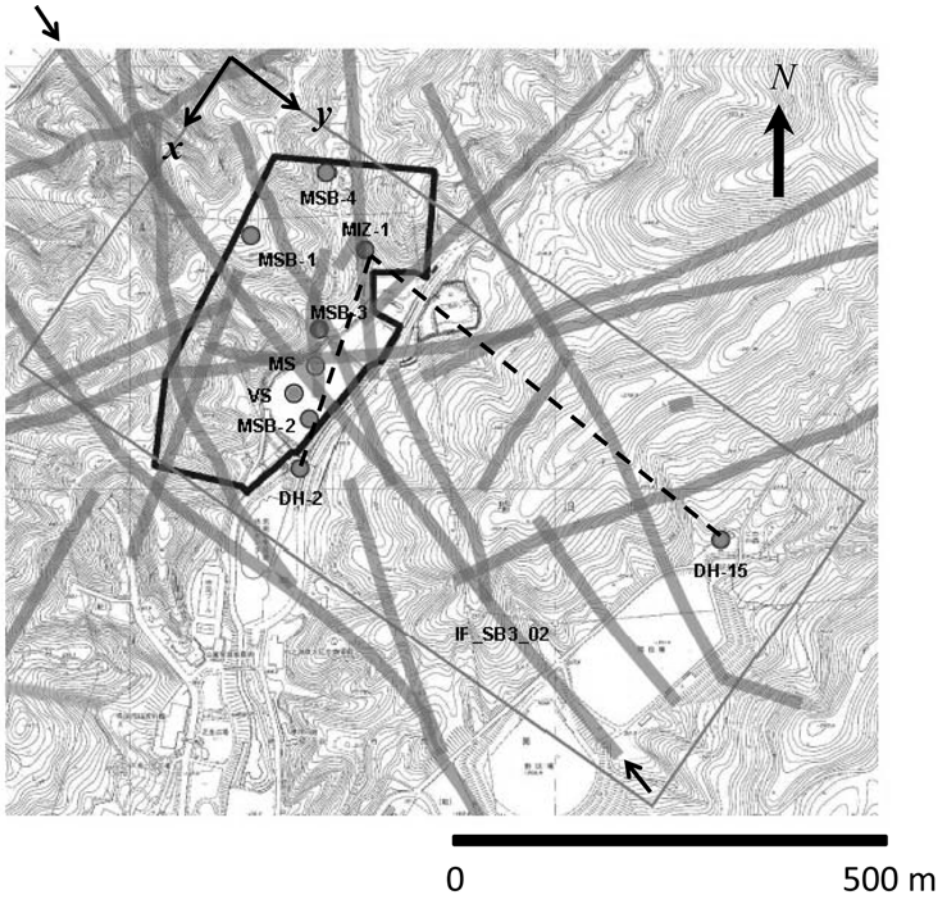

Figure 2. Map of lineament and faults obtained on the basis of the lineament and seismic surveys in the vicinity of the MIU site, where borehole locations as well as the location of the main shafts (MS) and ventilation shafts are shown. IF_SB3_02 is a fault that has been found to act as a flow barrier, and its location is indicated with arrows. The dashed line depicts the cross section of Figure 1.

Currently, the underground research facility is under construction for deep subsurface scientific investigations. Two 1,000-m deep shafts and several drifts are currently being excavated for geoscientific research as well as development and assessment of deep subsurface engineering techniques. JAEA is carrying out a wide range of research in an effort to build a firm scientific and technological basis for geological disposal of high-level nuclear waste.

2.2. Site Geology and Investigations

[15] The MIU site lies at the border of Cretaceous plutonic rocks of the Ryoke Belt and Mesozoic sedimentary rock of the Mino Belt. The research galleries of the MIU are being constructed in the Cretaceous Toki Granite, which forms the basement complex in the area as shown in a conceptual cross-sectional view of the site (Figure 1; see Figure 2 for the location of the cross section). The site geology consists of the Miocene Mizunami sedimentary rock sequence and the underlying Toki granite. The Mizunami Group is divided into Akeyo Formation, Hongo Formation (AK/HG in Figure 1) and Toki Lignite–bearing Formation (TK in Figure 1). The Akeyo and Hongo Formations are at the top and composed of tuffaceous sandstone, mudstone, granular conglomerate and basal conglomerate. The Toki Lignite–bearing Formation is mainly composed of muddy sandstone, tuffaceous sandstone, granular conglomerate, lignite and basal conglomerate at the bottom [*Itoigawa*, 1980]. The contact between the Hongo formation and the Toki Lignite–bearing formation is conceptualized to be a flow barrier. Toki Granite, which underlies the Toki Lignite–bearing formation, is composed of coarse-to-medium-grained biotite granite. The granite is highly fractured at depths between 300–500 m with dips of fractures that are less than 30 degrees. Beneath the highly fractured domain (upper highly fractured domain: UHFD in Figure 1) is a granitic body which is less fractured (lower sparsely fractured domain: LSFD in Figure 1), which is known to extend to large depths. Previous research and geological investigations at the site have shown that there are low-angle fracture zones (LAFZ in Figure 1) within the UHFD. In addition, there is evidence of the existence of various flow barriers (fault zones) including a prominent one that runs through the site oriented North-North-West (NNW) designated as fault IF_SB3_02.

[16] Within the MIU construction site boundary, numerous lineaments and potential fracture zones have been identified through lineament and seismic surveys. Figure 2 shows a plan view of the site map with the locations of the

boreholes, the locations of the main (MS) and ventilation shafts (VS), and the approximate extent of fault IF_SB3_02. In particular, this fault was recognized during early site mapping at a roadside outcropping and at a preexisting underground tunnel network as being potentially significant to groundwater flow because of the occurrence of fault gouge. The fault appears to be a normal fault, dipping approximately 85 degrees with about one meter of vertical displacement observed at the road cut, while the lateral displacement is unknown at this time. It has been intersected by borehole MSB-3 and by the main shaft. The fault has not been located in the northwest edge of the site. This fault can be seen to effectively compartmentalize the site into northeast and southwest regions. The hydrogeologic characteristics of these lineaments and faults, including those for fault IF_SB3_02, are largely unknown.

2.3. Description of Boreholes at the Site

[17] There are 7 vertical and slanted boreholes (MIZ-1, DH-2, DH-15, MSB-1, MSB-2, MSB-3, MSB-4, see Figure 2) in the area, in which various hydraulic tests have been conducted to date. The deep MIZ-1 borehole (1,300 m) was drilled to investigate the geological conditions at large depths. In addition, the site consists of 100 to 200-m long shallow boreholes (MSB-1 $\sim$ MSB-4) which penetrate the shallower sedimentary layers, but not the deeper granite. Additional off-site boreholes DH-2 and DH-15 were drilled to investigate the regional hydrogeology [*Power Reactor and Nuclear Fuel Development Corporation*, 1997]. In particular, DH-2 is situated on the southern boundary of the site with a depth of 500 m [*Doughty et al.*, 2005]. Borehole DH-15 is situated approximately 500 m southeast from the site, completed to a depth of 1,000 m. Previous research utilizing these boreholes has revealed the presence of the IF_SB3_02 fault. This fault has shown to abruptly change the groundwater pressures in the subsurface across the fault boundary, which has led *Kumazaki et al.* [2003] and *Salden et al.* [2005] to posit the presence of a low hydraulic conductivity barrier (LKB).

[18] Boreholes MSB-1, -2 and -4 were drilled vertically to investigate the properties of the sedimentary formations and top of the granite located within the MIU construction site boundary. They were drilled using continuous coring methods to the top of the granite. Borehole MSB-3 is an inclined borehole oriented to intersect a fault that had been identified by surface mapping and geophysical surveying. The fault was encountered at a depth of 87.7 to 92.2 m. At this location, the fault core is 0.3 m in width and consists of gouge and fault breccias [*Kumazaki et al.*, 2003].

2.4. Borehole Instrumentation

[19] The boreholes used in this study were instrumented with multilevel monitoring systems. Where the multilevel monitoring system separates a borehole into five isolated intervals, we append to the borehole designation a suffix 1, 2,...5 to identify the various intervals, i.e., MSB1–1, MSB1–2,..., and MSB1–5. We note that the higher the suffix number, the deeper the observation interval. For example, the borehole interval monitored by MSB1–1 ranges from 66.6–116.5 mbgs, while for MSB1–5, the interval ranges from 196.2–201.2 mbgs.

[20] The four MSB series wells were instrumented with MP Systems® manufactured by Westbay Instruments Inc. Monitoring wells MSB-1 and MSB-3 were instrumented with pressure transducers and data loggers. Groundwater pressures (and barometric pressure) have been recorded since December 2002 from a total of 12 monitoring zones in these two wells. Data were recorded typically once every 5 min to 30 min. Monitoring wells MSB-2 and MSB-4 were primarily water sampling wells, but have had pressure measured with a manually deployed pressure probe approximately monthly. The monitoring systems of these monitoring wells are a ''closed system'' with the pressure sensors located at the monitoring zone. These closed systems result in a very low time lag which makes the system suitable for measuring locations with very low hydraulic conductivity. DH-2 was instrumented with a 7-zone multilevel standpipe monitoring system (i.e., an ''open system'') in December 2002. This was replaced in November 2004, with a 12-zone MP System®. DH-15 was instrumented with a 10-zone multilevel standpipe monitoring system and data loggers. Groundwater pressures (and barometric pressure) have been recorded since November 2004.

3. Design of Cross-Hole Pumping Tests

[21] Two cross-hole pumping tests were conducted: one with pumping taking place in borehole MIZ-1 at depth intervals of 191–226 m and the other at 662–706 m, while monitoring of water pressure took place in numerous packed-off intervals in neighboring boreholes, DH-2, DH-15, MSB-1 and MSB-3, which have 12, 10, 5 and 7 observation intervals respectively. These two pumping intervals were selected because of fracture zones known from borehole surveys intersecting them. From now on, we refer to the pumping test at the shallower interval as test 1 and at the deeper interval as test 2. Test 1 was conducted at the Low-Angle Fracture Zone (LAFZ), in order to estimate the hydraulic characteristics of the LAFZ and its connectivity with surrounding monitoring wells (S. Takeuchi et al., Study on hydrogeological conceptualization in a fractured rock based on the cross-hole hydraulic test: Identification of site-scale compartment structure and preferential water-conducting feature (in Japanese), submitted to *Journal of the Japan Society of Engineering Geology*, 2008). Test 2 was designed to investigate the suspected connectivity of the large fault zone between boreholes MIZ-1 and DH-2 and its hydraulic characteristics (S. Takeuchi et al., submitted manuscript, 2008). Both cross-hole pumping tests utilized instruments that are designed for high pressure conditions at 2,000 m depth from the ground surface. Test 1 began on 14 December 2004 and lasted until 28 December 2004 with an average pumping rate of 10.8 L/min. Test 2 began on 13 January 2005 and lasted until 28 January 2005 with an average pumping rate of 5.2 L/min. Upon completion of both cross-hole tests, the pressure was allowed to recover in all intervals.

[22] Prior to the beginning of the long-term cross-hole pumping tests, there was a concern of the invasion of the drilling mud causing a mud cake around the pumped intervals, thus the pumping well was developed by performing pulse and slug tests, as well as short-term constant rate pumping tests. The well development appears to have removed the mud cake formed at the pumping intervals. This is evident from the recovery of the water levels not shown here. The pulse withdrawal and short-term

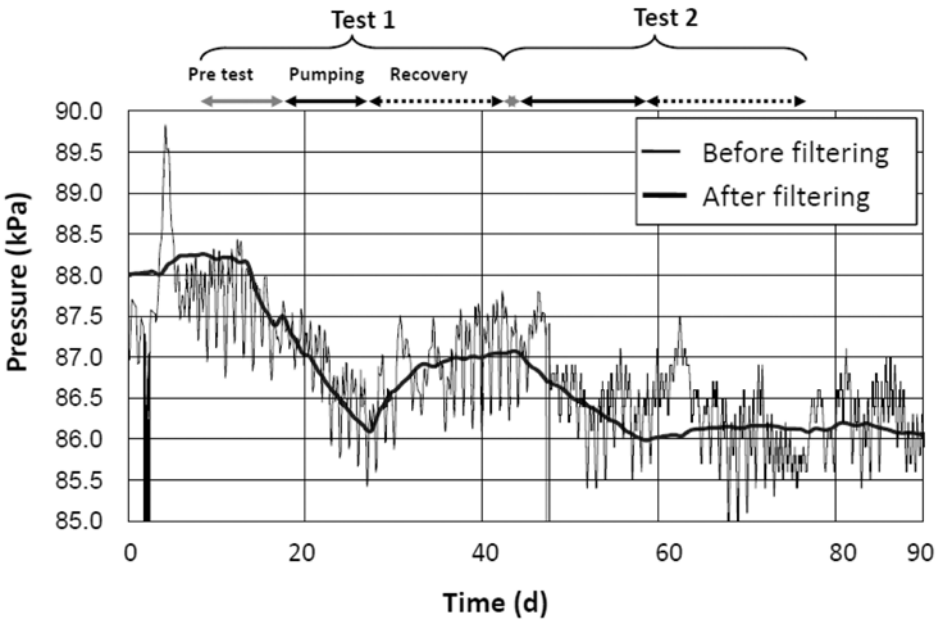

Figure 3. Pressure variation in an observation interval showing an example of data set prior to and after filtering/noise removal (after S. Takeuchi et al., submitted manuscript, 2008).

constant rate tests completed prior to the long-term continuous cross-hole pumping tests were not used in the subsequent analysis for this project.

4. Cross-Hole Pumping Test Results

[23] The pumped and observed packed-off intervals, as well as subsurface geological conditions in relation to the boreholes have been shown in Figure 1. We indicate the observation intervals which showed a strong/clear response through dark solid circles on Figure 1 during the two cross-hole tests. We found that the response was on the order of 2 kPa (hydraulic head ~20 cm) in many of the intervals. Prior to the interpretation of the data, they were first processed in order to remove Earth tide [*Robinson*, 1939; *Bredehoeft*, 1967] as well as barometric pressure variation effects to extract the drawdown signals due to pumping (Figure 3).

[24] During the two pumping tests, we were able to obtain a strong response in the deeper intervals located in borehole MSB-1 as well as all observation intervals in borehole DH-15. On the other hand, borehole DH-2 situated on the west side of fault IF_SB3_02 (as well as intervals placed above the fractured granite in the sedimentary sequence in borehole MSB-1) did not register strong water level variations in response to the two pumping tests while in MSB-3, responses varied considerably.

5. Inverse Model Description

[25] This section describes our efforts on application of the THT inverse code (Sequential Successive Linear Estimator, SSLE) of *Zhu and Yeh* [2005] to the pumping tests that took place at two intervals in borebole MIZ-1 and pressure data that were collected at four surrounding boreholes DH-2, DH-15, MSB-1 and MSB-3.

[26] The rectangular domain shown on Figure 2 selected for the THT analysis has x, y, z dimensions of 884 m × 392 m × 1054 m. It was discretized into 4216 elements and 5184 nodes with element dimensions of 52 m × 49 m × 34 m. Initial conditions were set by assuming that groundwater was static prior to the beginning of each cross-hole test. The top boundary was set to be a constant head boundary, while all other boundaries were considered to be no-flow boundaries. Additional simulations not shown here showed that the treatment of the side and bottom boundaries as no-flow boundaries did not affect the inversion results significantly. A similar conclusion was reached by *Vesselinov et al.* [2001a, 2001b], but they conducted pneumatic tomography using shallow boreholes in unsaturated fractured rocks, which is considered to be more conductive.

5.1. Description of Model Input Parameters

[27] Inputs to the THT model include guesses for the mean K and S_s values, estimates of variances and the correlation scales for both parameters, volumetric discharge (Q_n) from each pumping test where n is the test number, available point (small-scale) measurements of K and S_s, as well as head data at various times selected from the head time curve. Although available point (small-scale) measurements of K and S_s can be input to the model, we do not use these measurements to condition the estimated parameter fields to test the inversion algorithm.

5.2. Hydraulic Parameters K and S_s

[28] A number of methods can be used to estimate the mean values of K and S_s. One can set an arbitrary value that is reasonable for the geologic medium considered or to estimate the equivalent or effective hydraulic conductivity (K_{eff}) and specific storage (S_{seff}) for an equivalent homogeneous geologic medium. If there are small-scale data available, then a geometric mean of the available small-scale data (i.e., core, slug, and single-hole data) can be calculated. An alternative is to use the equivalent hydraulic conductivity and specific storage estimates obtained through the analysis of cross-hole test data by treating the medium to

Table 1. Observation Intervals and the Number of Data Utilized in THT During Cross-Hole Test 1 and 2

Observed Interval	Number of Measurements Used in Pumping Test 1	Number of Measurements Used in Pumping Test 2
MSB1−1	4	0
MSB1−2	0	0
MSB1−3	6	7
MSB1−4	7	7
MSB1−5	0	0
MSB3-1	0	0
MSB3-2	0	0
MSB3-3	6	0
MSB3-4	6	0
MSB3-5	6	0
MSB3-6	6	0
MSB3-7	6	0
DH2-1	6	0
DH2-2	0	0
DH2-3	6	0
DH2-4	5	0
DH2-5	6	0
DH2-6	0	0
DH2-7	5	0
DH2-8	0	0
DH2-9	5	0
DH2-10	4	0
DH2-11	0	0
DH2-12	0	0
DH15-1	7	7
DH15-2	8	7
DH15-3	5	7
DH15-4	5	0
DH15-5	7	7
DH15-6	5	7
DH15-7	6	7
DH15-8	7	7
DH15-9	7	7
DH15-10	0	7

be homogeneous. We elected to utilize the geometric mean values of equivalent K (1.0×10^{-2} m/d) and S_s (2.3×10^{-6} m^{-1}) obtained through the asymptotic analysis [*Illman and Tartakovsky*, 2006] of test 1.

5.3. Variance and Correlation Scales

[29] The variances and correlation scales of the K and S_s fields are also required inputs to the THT model. We obtain variance estimates from the results of the asymptotic analysis of cross-hole test 1 ($\sigma^2_{\ln K} = 2.0$ and $\sigma_{\ln S_s}{}^2 = 0.5$) and use them as the input variances in the inverse model for the THT analysis of tests 1 and 2. It is a well-known fact that variance estimation always involves some uncertainty. A previous numerical study conducted by *Yeh and Liu* [2000], nevertheless, has shown that the variance has negligible effects on the estimated K on the basis of data from HT. This is also true for the K and S_s estimates based on data from THT [*Zhu and Yeh*, 2005, 2006; *Liu et al.*, 2007].

[30] Correlation scales represent the average size of the dominant heterogeneity (in this case, average length of fractures) in the geologic medium. They are often difficult to determine accurately without a large number of hydraulic property measurements or a detailed map of fracture distribution in the medium. The correlation scales for this investigation were approximated, on the basis of observed lineaments, to be 50 m in both horizontal and vertical directions, while an exponential model was assumed for the THT analysis. While these estimates are uncertain, the effects of uncertainty in the correlation scales on the estimate based on the tomography are generally negligible because a tomographic survey collects a large number of head measurements, which already bear information of the detailed site-specific heterogeneity [*Yeh and Liu*, 2000].

5.4. Transient Hydraulic Head Data

[31] Transient hydraulic head records are required for THT. These were obtained from observation intervals that yielded data that were not too noisy and were treated with various error reduction schemes discussed by *Illman et al.* [2007]. Briefly, the error reduction schemes consisted of accounting for pressure transducer drift and removal of data affected by skin effects.

[32] Selection of observation interval data for THT analysis consisted of examining the pumping records and the corresponding changes in hydraulic head. We primarily utilized data that showed a strong response to pumping in MSB-3 and DH-15. Data from observation intervals in MSB-1 and DH-2 were also utilized even if they were considered to be weak responses to pumping, if they were not overwhelmed by noise and if they appeared to be due to pumping. We excluded data that did not exhibit clear response to pumping. This was because the observation interval data with small or zero responses were usually overwhelmed by external factors at this site, which the inverse model did not explicitly account for. In this investigation, inclusion of small or zero response data (i.e., low signal-to-noise ratio) into the inverse model could have resulted in the overinterpretation of the available data, although others have found it to be useful because it provides information on fracture connectivity or lack of it [*Day-Lewis et al.*, 2000].

[33] We also did not use data from borehole DH2 (DH2−1 ∼ DH2−12) from test 2 even though the intervals showed small responses to pumping. We excluded these data to later use it for validation purposes [e.g., *Illman et al.*, 2007, 2008; *Liu et al.*, 2007]. That is, the K and S_s tomograms computed will be used to predict the drawdown responses for intervals in borehole DH2 during test 2 to assess the validity of the tomograms.

[34] The 3-D grid used for the inverse modeling was designed to be relatively coarse to facilitate the efficient computation of the tomograms while allowing for the capturing of large-scale features at the site. This caused some of the neighboring observation intervals to be collocated in a single grid block. For example, MSB1−4 and MSB1−5 were collocated in a single grid block. We included data from MSB1−4, but not from MSB1−5 into the THT analysis, because the data appeared similar for both tests. Several other data sets from other observation intervals (DH2−2, DH2−6, and DH2−8) were not included in the THT analysis for the same reasons.

[35] After careful selection of data, we calculated drawdown for each observation interval during a pumping test. We then extracted 4 to 7 points to represent the entire drawdown curve and to represent the transient behavior thoroughly. In total, we utilized two independent cross-hole tests which were at our disposal for the THT analysis. More specifically, we utilized 141 drawdown records from 24 observation intervals in test 1 and 77 drawdown data from 11 observation intervals in test 2. In summary, we utilized

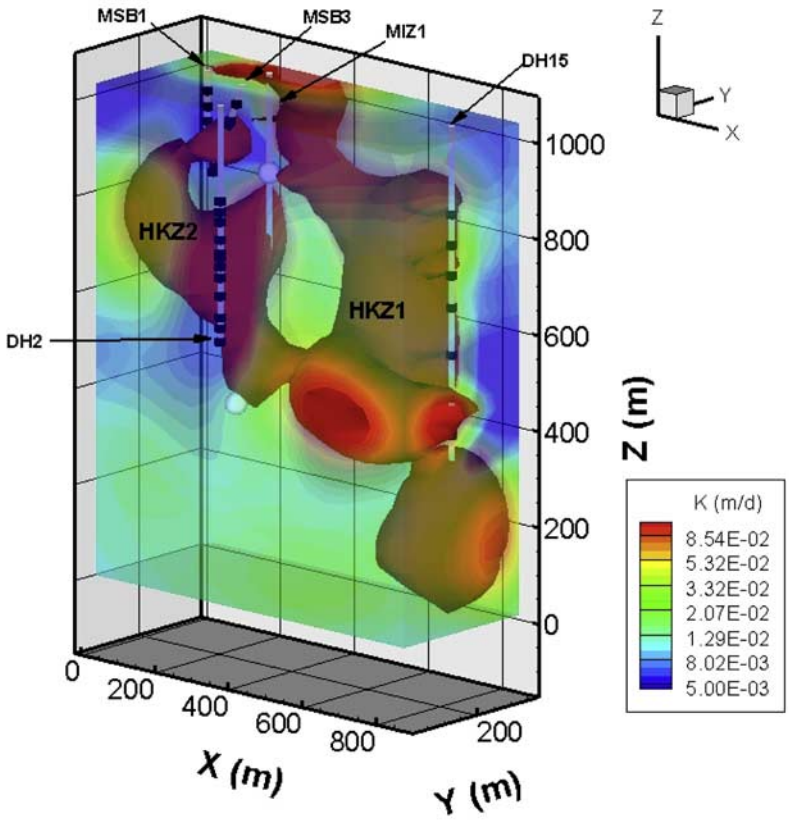

Figure 4. Three-dimensional K tomogram (m/d) obtained from the inversion of two cross-hole tests. Pumped locations are indicated by solid white spheres, while observation intervals are indicated by solid black squares.

218 drawdown records from two different tests in our transient inversions. Table 1 summarizes the number of data extracted from each observation interval for tests 1 and 2.

6. Results of Analysis of Two Cross-Hole Pumping Tests

6.1. Hydraulic Conductivity, Specific Storage Tomograms, and Their Uncertainty Estimates

[36] Figure 4 shows the estimated K field in 3-D, which reveals several high K zones that appear to be connective. Here, we refer to well connected fracture sets imaged by THT as the continuous high K region above a cutoff value of 0.1 m/d (shown in red on Figure 4; see also Figure 11). Results not presented here show that there is a moderate negative correlation between K and S_s implying that regions of high K/low S_s or high diffusivity could potentially also delineate the connectivity of fractures at a given site.

[37] Examination of Figure 4 shows that one high K zone extends from near the shallower pumping location (MIZ1–1) toward borehole DH-15, which we refer to as high K zone 1 (HKZ1). There is also another high K zone that extends from the deeper pumping location (MIZ1–2) to the bottom of borehole MSB-3, which we refer to HKZ2. HKZ1 and HKZ2 are connected at approximately 500 m below the top of the tomogram. Figure 5 shows the corresponding estimation variance of ln-K revealing that uncertainty in the K estimate is generally lower in the region near the pumped and observation intervals. Interestingly, the estimation variance was also found to be lower within a portion of HKZ1, however, we do not speculate on its correlation.

[38] Figure 6 shows the corresponding S_s distribution revealing two regions of lower S_s generally corresponding with the high K zones, while Figure 7 shows the corresponding estimation variance of ln-S_s. Comparisons of these K and S_s distributions and the local geology as well as hydraulic behavior in observation intervals during the two cross-hole tests show that these regions may be defining a fracture/fault zone of the site.

[39] The K and S_s tomograms (Figures 4 and 6) at the MIU site are likely smoother than the true heterogeneity distribution. We attribute the smoothness of the tomograms to the availability of two cross-hole tests and only a limited number of monitoring points within the 0.36 km^3 block of fractured rock investigated here. In addition, the borehole configuration [*Menke*, 1984] as well as other factors cited by *Day-Lewis et al.* [2005] could have impacts on tomogram resolution. We anticipate that a more accurate geometry of fractures and fault zones will emerge as more cross-hole pumping test data are conducted strategically and included into the THT algorithm.

[40] A previously conducted synthetic study [*Hao et al.*, 2008] showed that hydraulic tomography can define fracture zones and fracture connectivities on the basis of the

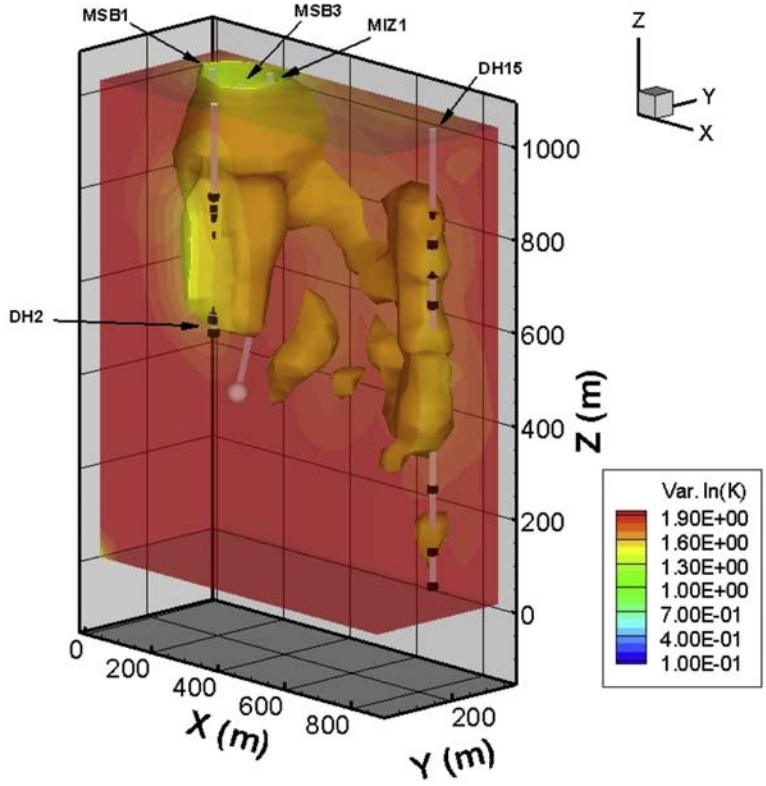

Figure 5. Three-dimensional distribution of the estimation variance of ln K resulting from the inversion of two cross-hole tests. Pumped locations are indicated by solid white spheres, while observation intervals are indicated by solid black squares.

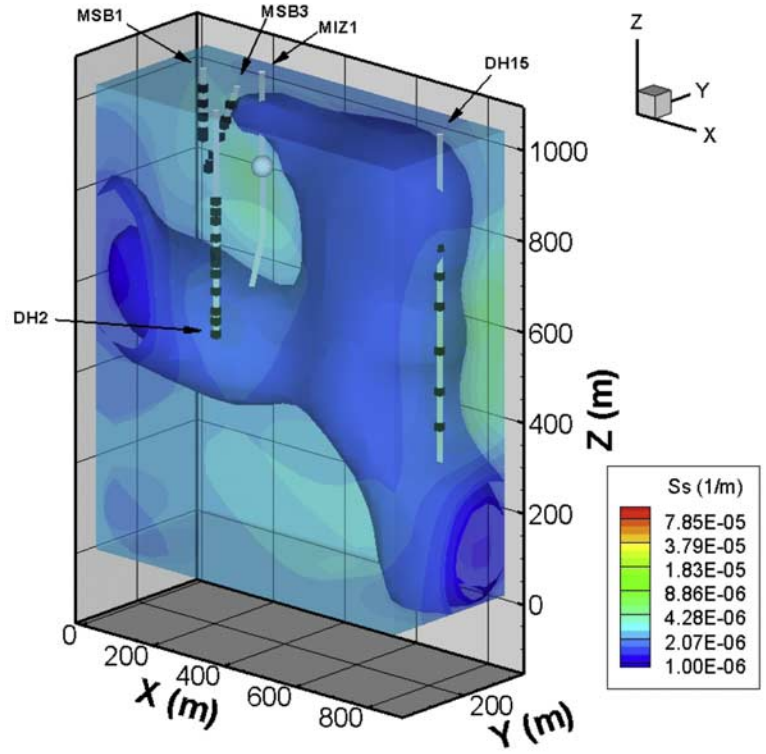

Figure 6. Three-dimensional S_s tomogram (per m) obtained from the inversion of two cross-hole tests. Pumped locations are indicated by solid white spheres, while observation intervals are indicated by solid black squares.

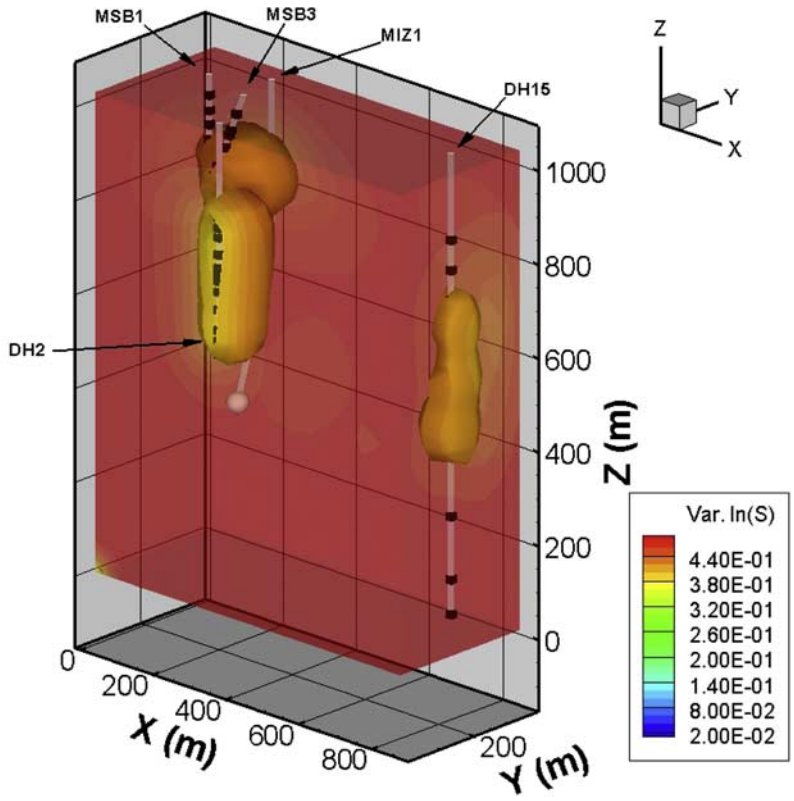

Figure 7. Three-dimensional distribution of the estimation variance of ln S_s resulting from the inversion of two cross-hole tests. Pumped locations are indicated by solid white spheres, while observation intervals are indicated by solid black squares.

pattern of K estimates. On the other hand, the pattern of S_s estimates does not reflect the synthetic fracture patterns as clearly as that of K estimates. In addition, they showed that estimated K and S_s values for the fracture become close to the true ones and that fracture pattern and connectivity can be vividly delineated if a larger number of observation intervals are utilized and as more cross-hole tests are conducted with pumping taking place at different locations. Inclusion of additional cross-hole tests at the MIU site, therefore, should reveal the pattern and properties of fracture zones more vividly and reduce the uncertainties in our estimates.

[41] Previously, *Illman et al.* [2008] found through the inversion of laboratory sandbox data that the order of test

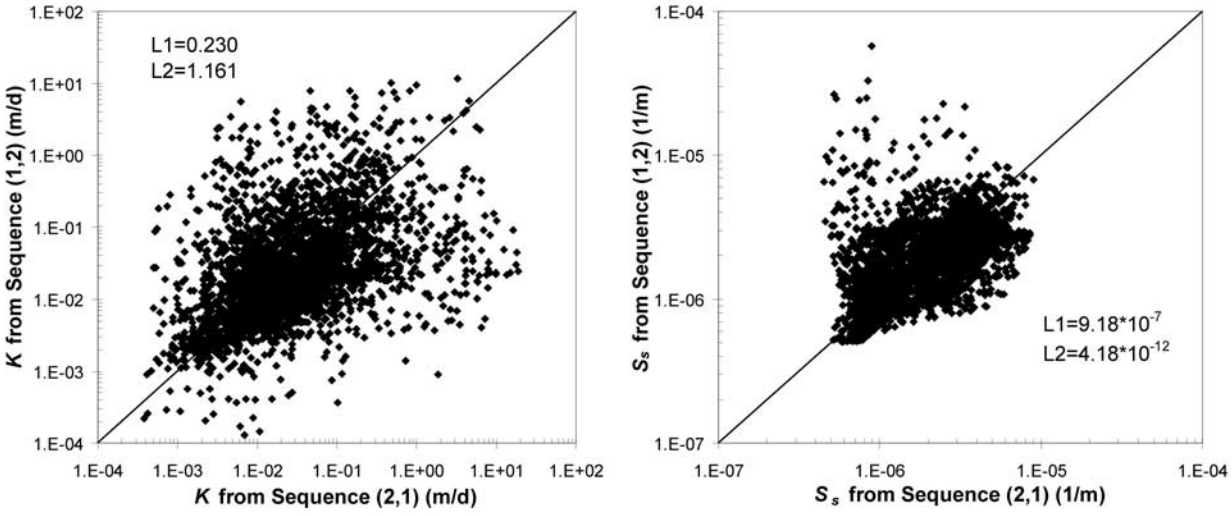

Figure 8. Scatter plots of local (a) K and (b) S_s values from sequence 1 (test 1 and 2, in that order) to sequence 2 (test 2 and 1, in that order).

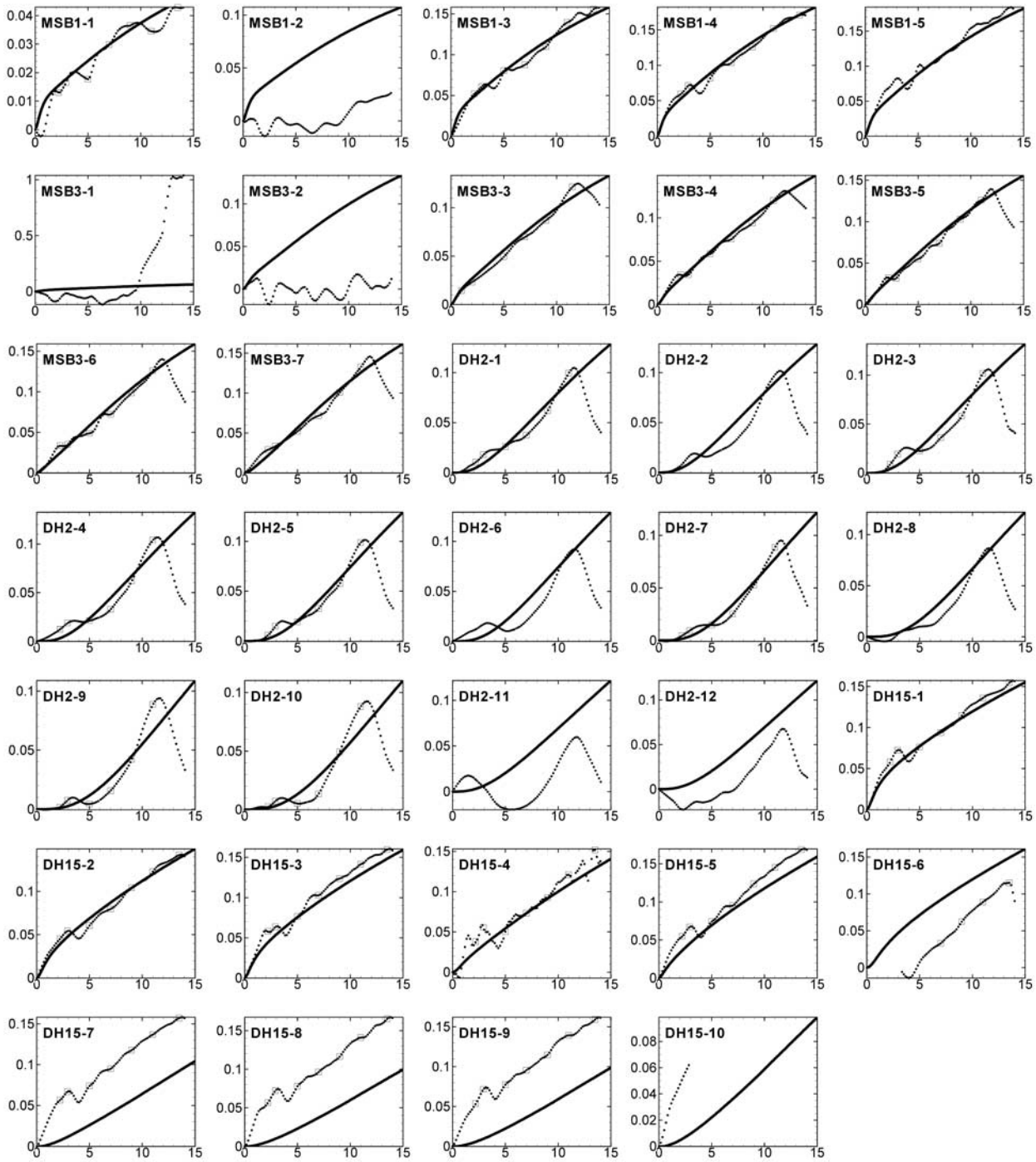

Figure 9. Observed (small dots) and calibrated (curves) records of drawdown (m) versus time (days) during cross-hole pumping test 1. Drawdown data input into the THT algorithm are indicated as open squares.

data included into the SSLE could have an impact on the quality of K tomogram using the HT algorithm of *Yeh and Liu* [2000]. In particular, these authors showed that including the data with the highest signal-to-noise ratio first into the HT code and including the data with the lowest signal-to-noise later appeared to improve the results. The main reason for this is because SSLE uses a weighted linear combination of the differences between the estimated heads and measured heads to improve the tomogram. Therefore, an unrefined K distribution obtained in the beginning of inversion process will generate larger differences between the estimated and measured heads than a refined K distribution causing the inverse solution to become unstable as additional data are included into SSLE. Therefore, including the cleanest data with higher signal-noise ratio in the beginning of the inversion process tends to improve the results.

[42] In this study, the K and S_s tomograms (Figures 4 and 6) were obtained by including selected data from test 1 and 2 into the SSLE, in that order. We also reversed the order of test data input into the THT algorithm to examine the robustness of the K and S_s tomograms. Figures 8a and 8b show scatterplots of local K and S_s values, respectively, from sequence 1 (test 1 and 2, in that order) to sequence 2 (test 2 and 1, in that order). Two criteria, the average absolute error norm (L1) and the mean squared error norm (L2) were used to quantitatively evaluate the goodness-of-fit between the two sets of tomograms:

$$L_1 = \frac{1}{n}\sum_{i=1}^{n}|\chi_i - \hat{\chi}_i| \quad (1)$$

$$L_2 = \frac{1}{n}\sum_{i=1}^{n}(\chi_i - \hat{\chi}_i)^2 \quad (2)$$

where χ_i and $\hat{\chi}_i$ represent the parameter (either K or S_s) from sequence 1 and 2, respectively, i indicates the element number, and n is the total number of elements. The smaller the L1 and L2 norms are, the more consistent are the estimates. These results show that reversing of the order of data inclusion into the SSLE does not significantly impact the quality of the K and S_s tomograms. The tomograms were found to be not adversely impacted by reversing the order of test data included into the THT algorithm because the signal-to-noise ratio of each test was found to be on the same order of magnitude and that there are only two pumping tests available for the THT analysis.

7. Evaluation of K and S_S Tomograms

[43] Here, we describe three independent approaches to evaluate the soundness of the estimated fracture K and S_s patterns on the basis of (1) the comparison of calibrated and observed drawdown records including the prediction of drawdown responses from intervals not used in the construction of the tomograms, (2) the comparison of tomograms to known fault locations, and (3) the use of coseismic groundwater level responses during several large earthquakes.

7.1. Comparison of Calibrated and Observed Drawdown Records From Transient Hydraulic Tomography: Tests 1 and 2

[44] Figure 9 compares observed (dots) and calibrated (solid curves) records of drawdown versus time in 34 intervals during cross-hole test 1. Drawdown data input into the THT algorithm are also included in this plot as open squares. Similar comparisons are provided in Figure 10 for test 2. Drawdown records from intervals DH2–1 through DH2–12 during test 2 were not used in the inverse modeling effort but are plotted in Figure 10 to show that the K and S_s tomograms do a reasonably good job in predicting the drawdown responses. Overall, most of the simulated responses capture with reasonable fidelity the observed drawdown behaviors in these intervals. Some of the matches are very poor, some are of intermediate quality, and some are good to excellent. This result is expected as the inability of our inverse model to reproduce all drawdown records stems in part from (1) the representation of a heterogeneous rock through a coarse grid; (2) the conditional effective estimates from the THT inverse model; (3) discrepancies between the true and modeled initial and boundary conditions; (4) the model disregarding borehole storage, skin, and non-Darcy flow in fractures [*Day-Lewis et al.*, 2000]; and (5) in part from extraneous signals such as Earth tides and ambient groundwater flow that our inverse model does not attempt to reproduce.

7.2. Use of Available Fault and Lineament Data

[45] We next evaluate the tomograms by comparing them to available fault and lineament data collected at the MIU site [*Onoe et al.*, 2007]. This information was obtained through surface mapping, lineament and seismic surveys. Additional data utilized to map the faults include fracture density and fault locations obtained along the boreholes and in the main and ventilation shafts, which are currently under construction.

[46] The evaluation procedure consists of questioning whether the computed tomograms make any geological sense or not. That is, do the high K zones on the tomograms correspond with locations of faults and lineaments that have been mapped independently? To answer this, we plot the major fault zones one-by-one into the K tomograms (Figures 11a, 11b, 11c, 11d, 11e, and 11f) to see any correlation. We recognize that this comparison is qualitative because available fault data do not provide us with information on hydrogeologic properties. That is, some faults may be conductive, while others may act as flow barriers. Despite the qualitative nature of the analysis, any correspondence between the tomograms and the fault zone data should give us more confidence in our results.

[47] Figure 11a, 11b, 11c, 11d, 11e, and 11f shows 3-D isosurfaces of K obtained from the same K tomogram shown earlier (Figure 4). The red isosurface (K = 0.1 m/d) is shown to highlight the high K zones, while the blue isosurface (K = 0.005 m/d) is shown to highlight the low K features. High K zones 1 and 2 (HKZ1 & HKZ2) indicated in Figure 4 and the low K barrier (LKB) are highlighted on various plots. The black dots comprising a curved plane delineate faults and lineaments.

[48] In particular, Figure 11a shows that fault IF_SB3_15 passes the region under MIU and intersects the high K zone 1 (HKZ1). It appears from examining Figures 11a and Figure 11b that another fault L171 intersects fault IF_SB3_15 and forms part of the HKZ1. Likewise, Figure 11c reveals that fault IF_SB3_13_2_1 passes through the high K zone 2 (HKZ2) which effectively connects the lower pumped interval (MIZ1–2) to the deep intervals of boreholes MSB-1. It is of interest to note that the fault locations correspond with high K zones but the latter are not planar. In addition, the local K values within the faults may be spatially variable, thus ascribing a constant K value for a given fault may not be justified [e.g., *Bear et al.*, 1993; *NRC*, 1996].

[49] We see from Figure 11d and results that we discuss later that not all faults are conductive. Figures 11d and 11e show fault IF_SB3_02 and IF_SB3_02_01 forming a low K barrier (LKB) between boreholes DH-2 and MSB-1/3 as well as borehole MIZ1. IF_SB3_02 is a larger and more continuous fault while IF_SB3_02_01 is a smaller LKB. Finally, Figure 11f shows another fault IF_SB0_03 intersecting the LKB.

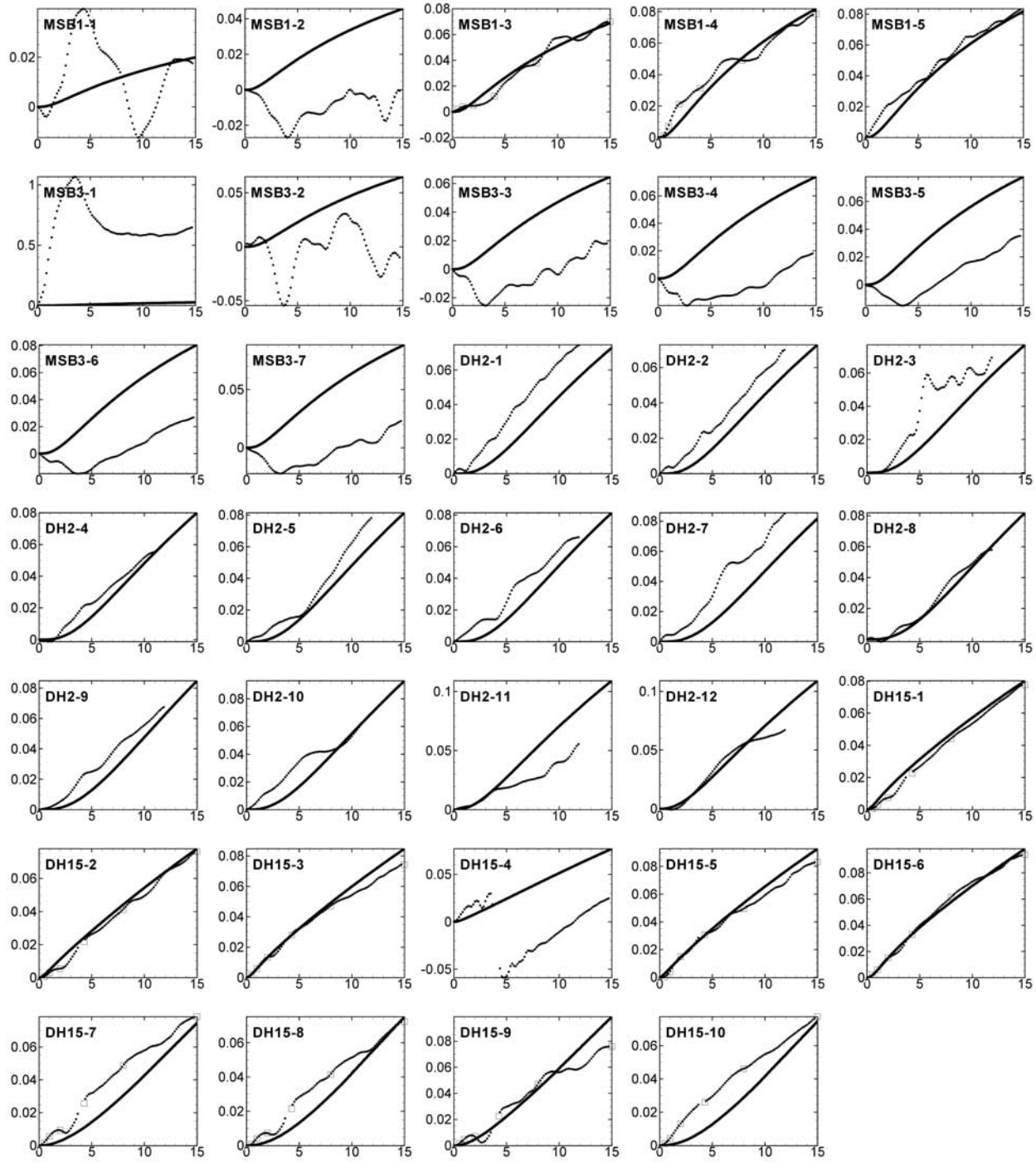

Figure 10. Observed (small dots) and calibrated (curves) records of drawdown (m) versus time (days) during cross-hole pumping test 2. Drawdown data input into the THT algorithm are indicated as open squares.

[50] Our examination of the fault and lineament data revealed that there are also several other fault zones not showing up on the tomograms which could be due to a number of factors such as (1) THT did not detect some of the fracture/fault zones because of a small number of pumping tests and monitoring wells available for our analysis; (2) that some of these suspected fracture zones are filled with fault gouges, thus are not very conductive and consequently do not appear as high K and low S_s features on the tomograms; and (3) that the fracture/fault zones do not extend far from the borehole.

7.3. Use of Coseismic Groundwater Pressure Changes

[51] We next utilize coseismic groundwater pressure changes as a means to evaluate the tomograms. In particular, the difference in pressure responses to the two cross-hole pumping tests across the IF_SB3_02 fault zone (Figure 12;

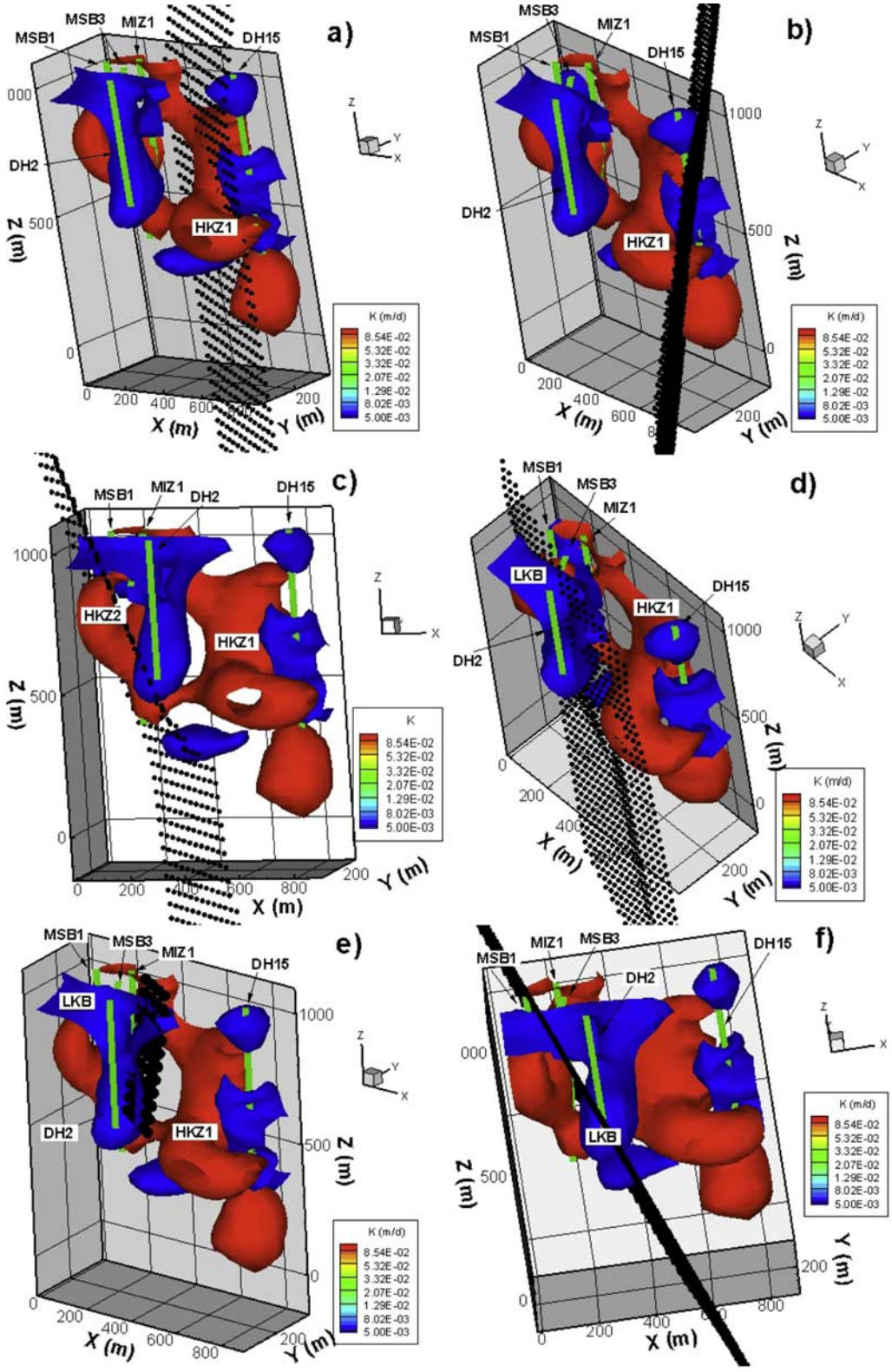

Figure 11. Three-dimensional isosurfaces obtained from the *K* tomogram (Figure 4) with available fault and lineament data (black dots) included. The red isosurface ($K = 0.1$ m/d) is shown to highlight the high *K* zones, while the blue isosurface ($K = 0.005$ m/d) is shown to highlight the low *K* features. (a) Fault IF_SB3_15 intersects the high *K* zone 1 (HKZ1). (b) Fault L171 intersects fault IF_SB3_15 and forms part of the HKZ1. (c) Fault IF_SB3_13_2_1 connects the lower portion of MIZ2 and the deeper intervals of MSB1 and MSB3, forming high *K* zone 2 (HKZ2). (d) Fault IF_SB3_02 forms a low *K* barrier (LKB) between DH2 and MSB1/3, MIZ1. (e) Fault IF_SB3_02_01 is a smaller fault which is part of the LKB that exists between DH2 and MSB1/3, MIZ1. (f) A section of fault: IF_SB0_03 intersecting the LKB.

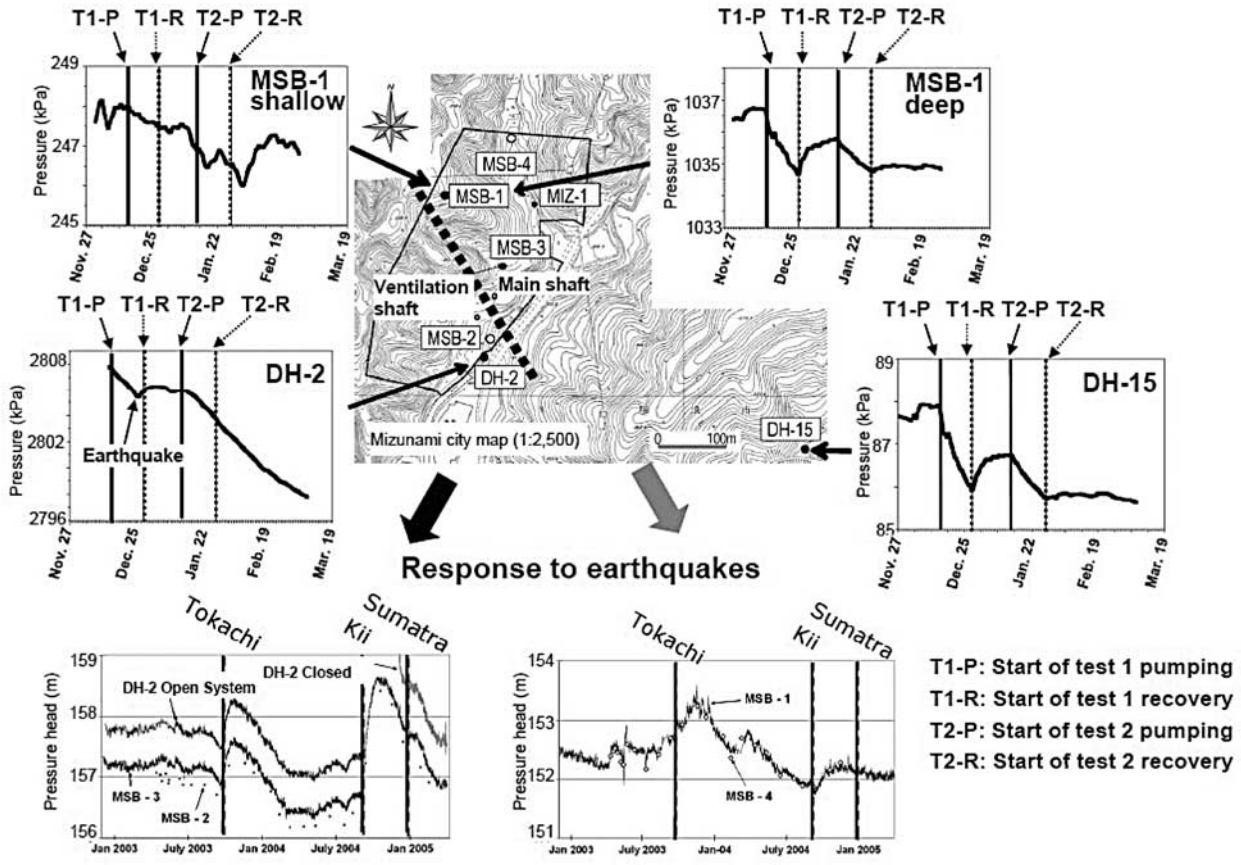

Figure 12. Pressure responses in selected observation intervals due to cross-hole pumping tests 1 and 2 as well as coseismic responses during the Tokaichi, Kii, and Sumatra earthquakes at the MIU site (after S. Takeuchi et al., submitted manuscript, 2008).

see also Figures 11d and 11e) is also corroborated by the coseismic response variations due to recent earthquakes (Tokachi, Magnitude (M) = 8.0; Kii, M = 7.4; Sumatra-Andaman, M = 9.2) that have occurred during the period of 2002–2005. For example, large and clear pressure responses due to pumping are observed on the northeast side of the IF_SB3_02 fault zone, such as in the deeper intervals of MSB-1 and nearly all intervals in DH-15 (Figure 12). However, responses to pumping are not visible in DH-2 observation intervals at the southwest side of the fault zone. We also note that the shallow intervals of MSB-1 do not respond to pumping (Figure 12). This is because of the suspected flow barrier between the Hongo formation and the Toki Lignite–bearing unit of the Mizunami sedimentary group (see Figure 1). On the other hand, the coseismic response of water pressure was not observed at observation intervals in boreholes MSB-1 and DH-15 on the northeast side of the IF_SB3_02 fault zone, but was seen clearly on the southwest side of the fault zone in DH-2 observation intervals. On the basis of all of this evidence, groundwater flow appears to be compartmentalized by the IF_SB3_02 fault zone and additional inferred low permeable faults from lineament surveys. Furthermore, a fault zone which was thought initially to connect boreholes MIZ-1 and DH-2 targeted by cross-hole pumping test 2 did not show a pressure response. Therefore, it is plausible that this particular fault zone does not connect the two boreholes or else the connection is so good that the K is very high causing the drawdown response to dissipate quickly. However, when we consider the differences in coseismic groundwater pressure changes and the differences in the pressure responses across the IF_SB3_02 fault zone, the former explanation appears to be more plausible at this time. These findings are consistent with the results of the estimated connectivity distribution by the THT.

8. Findings and Conclusions

[52] This study leads to the following major findings and conclusions regarding the THT analysis of cross-hole pumping tests 1 and 2 conducted at the Mizunami Underground Research Laboratory (MIU) construction site:

[53] 1. It is possible to interpret cross-hole pumping tests 1 and 2 using the THT code developed by *Zhu and Yeh* [2005]. In particular, the THT algorithm was able to image continuous high K and low S_s zones, which represent fast flow pathways and their connectivities. Here, we emphasize that there were only two cross-hole pumping tests for inversion purposes, but the computed K and S_s tomograms clearly show two fast flow pathways or conductive fault zones at the site. Clearer estimates of K and S_s as well as their connectivities should be obtained (and their uncertainties reduced) as additional cross-hole pumping tests are strategically conducted at the MIU site and included in the analysis.

[54] 2. We examined the robustness of the computed K and S_s tomograms by reversing the order of test data included into the THT algorithm. Results showed that tomograms obtained by switching the order of tests included in the THT algorithm were similar adding more confidence to the estimates. Here, we found the impact of the order of test data included into the THT algorithm appears to be small, because we only used two cross-hole pumping tests for the inversion and the quality of the drawdown records from the two pumping tests were found to be similar.

[55] 3. We then evaluated the K and S_s tomograms by examining the observed and calibrated records of water levels versus time during tests 1 and 2. We found that most calibrated responses captured with reasonable fidelity the observed drawdown behaviors.

[56] 4. Twelve drawdown records from borehole DH2 during cross-hole test 2 were excluded from the THT modeling effort to later use these data to evaluate the computed K and S_s tomograms. Results show that the predictions of drawdown records in those 12 observation intervals were good to excellent providing additional confidence in the validity of the computed K and S_s tomograms.

[57] 5. We also evaluated the K tomogram by comparing it to available fault and lineament data. In general, we found the major fault zones intersect the identified high K features. We also found the existence of low K features that are continuous which suggests that not all faults are conductive [e.g., *Bear et al.*, 1993; *NRC*, 1996]. These results suggest that the computed tomograms are consistent with available geological records providing us with further confidence in the validity of our results.

[58] 6. Finally, we utilized coseismic groundwater pressure changes as a means to evaluate the tomograms. In particular, the difference in pressure responses to the two cross-hole pumping tests across the NNW trending low K fault zone (IF_SB3_02) is corroborated by the coseismic response variations due to recent earthquakes that have occurred in the vicinity of Japan. We find that the large pressure response observed on the northeast side of the IF_SB3_02 fault zone due to pumping is not visible on the southwest side of the IF_SB3_02 fault zone. On the other hand, the coseismic response of water pressure was not observed on the northeast side of the IF_SB3_02 fault zone, but was seen clearly on the southwest side of the fault zone. On the basis of all of this evidence, groundwater flow appears to be compartmentalized by the IF_SB3_02 fault zone.

[59] 7. The results from the aforementioned approaches of evaluating the K and S_s tomograms are encouraging in that the tomograms are qualitatively consistent with other data that are available to us. More rigorous and quantitative means to evaluate the K and S_s tomograms are necessary. For example, *Illman et al.* [2007, 2008] and *Liu et al.* [2007] concluded that an appropriate validation approach is to test the predictability of head/drawdown fields using the estimated K and S_s fields under different flow scenarios. Perhaps, tracer experiments and geophysical surveys may be additional approaches that can substantiate the fracture zones identified in this study.

[60] **Acknowledgments.** This research was supported by funding from the National Science Foundation (NSF) through grants EAR-0229713, EAR-0229717, IIS-0431069, IIS-0431079, EAR-0450336, EAR-0450388, Strategic Environmental Research and Development Program (SERDP) through grant ER-1365, as well as the Discovery grant awarded to the senior author from the Natural Sciences and Engineering Research Council of Canada (NSERC). We thank the constructive reviews by Stephen Moysey, Tristan Wellman, an anonymous reviewer, and Frederick Day-Lewis, who was the associate editor assigned to this paper.

References

Andersson, J., and B. Dverstorp (1987), Conditional simulations of fluid flow in three-dimensional networks of discrete fractures, *Water Resour. Res.*, *23*(10), 1876–1886, doi:10.1029/WR023i010p01876.

Ando, K., A. Kostner, and S. P. Neuman (2003), Stochastic continuum modeling of flow and transport in a crystalline rock mass: Fanay-Augères, France, revisited, *Hydrogeol. J.*, *11*(5), 521–535, doi:10.1007/s10040-003-0286-0.

Bear, J. (1972), *Dynamics of Fluids in Porous Media*, 764 pp., Dover, New York.

Bear, J., C.-F. Tsang, and G. de Marsily (Eds.) (1993), *Flow and Contaminant Transport in Fractured Rock*, 560 pp., Academic, San Diego.

Benke, R., and S. Painter (2003), Modeling conservative tracer transport in fracture networks with a hybrid approach based on the Boltzmann transport equation, *Water Resour. Res.*, *39*(11), 1324, doi:10.1029/2003WR001966.

Berkowitz, B. (2002), Characterizing flow and transport in fractured geological media: A review, *Adv. Water Resour.*, *25*(8–12), 861–884.

Bibby, R. (1981), Mass transport of solutes in dual-porosity media, *Water Resour. Res.*, *17*(4), 1075–1081, doi:10.1029/WR017i004p01075.

Bohling, G. C., X. Zhan, J. J. Butler Jr., and L. Zheng (2002), Steady shape analysis of tomographic pumping tests for characterization of aquifer heterogeneities, *Water Resour. Res.*, *38*(12), 1324, doi:10.1029/2001WR001176.

Bohling, G. C., J. J. Butler Jr., X. Zhan, and M. D. Knoll (2007), A field assessment of the value of steady shape hydraulic tomography for characterization of aquifer heterogeneities, *Water Resour. Res.*, 43, W05430, doi:10.1029/2006WR004932.

Bonnet, E., O. Bour, N. E. Odling, P. Davy, I. Main, P. Cowie, and B. Berkowitz (2001), Scaling of fracture systems in geologic media, *Rev. Geophys.*, *39*(3), 347–383, doi:10.1029/1999RG000074.

Bour, O., and P. Davy (1998), On the connectivity of three-dimensional fault networks, *Water Resour. Res.*, *34*(10), 2611–2622, doi:10.1029/98WR01861.

Brauchler, R., R. Liedl, and P. Dietrich (2003), A travel time based hydraulic tomographic approach, *Water Resour. Res.*, *39*(12), 1370, doi:10.1029/2003WR002262.

Bredehoeft, J. D. (1967), Response of well-aquifer systems to Earth tides, *J. Geophys. Res.*, *72*(12), 3075–3087, doi:10.1029/JZ072i012p03075.

Butler, J. J., C. D. McElwee, and G. C. Bohling (1999), Pumping tests in networks of multilevel sampling wells: Motivation and methodology, *Water Resour. Res.*, *35*(11), 3553–3560, doi:10.1029/1999WR900231.

Cacas, M. C., E. Ledoux, G. de Marsily, A. Barbreau, P. Calmels, B. Gaillard, and R. Margritta (1990a), Modeling fracture flow with a stochastic discrete fracture network: Calibration and validation 1. The flow model, *Water Resour. Res.*, *26*(3), 479–489.

Cacas, M. C., E. Ledoux, G. de Marsily, A. Barbreau, P. Calmels, B. Gaillard, and R. Margritta (1990b), Modeling fracture flow with a stochastic discrete fracture network: Calibration and validation 2. The transport model, *Water Resour. Res.*, *26*(3), 491–500.

Cvetkovic, V., S. Painter, N. Outters, and J. O. Selroos (2004), Stochastic simulation of radionuclide migration in discretely fractured rock near the Äspö Hard Rock Laboratory, *Water Resour. Res.*, *40*, W02404, doi:10.1029/2003WR002655.

Darcel, C., O. Bour, P. Davy, and J. R. de Dreuzy (2003), Connectivity properties of two-dimensional fracture networks with stochastic fractal correlation, *Water Resour. Res.*, *39*(10), 1272, doi:10.1029/2002WR001628.

Day-Lewis, F. D., P. A. Hsieh, and S. M. Gorelick (2000), Identifying fracture-zone geometry using simulated annealing and hydraulic-connection data, *Water Resour. Res.*, *36*(7), 1707–1721, doi:10.1029/2000WR900073.

Day-Lewis, F. D., J. W. Lane Jr., J. M. Harris, and S. M. Gorelick (2003), Time-lapse imaging of saline-tracer transport in fractured rock using difference-attenuation radar tomography, *Water Resour. Res.*, *39*(10), 1290, doi:10.1029/2002WR001722.

Day-Lewis, F. D., K. Singha, and A. M. Binley (2005), Applying petrophysical models to radar travel time and electrical resistivity tomograms: Resolution-dependent limitations, *J. Geophys. Res.*, *110*, B08206, doi:10.1029/2004JB003569.

Day-Lewis, F. D., J. W. Lane, and S. M. Gorelick (2006), Combined interpretation of radar, hydraulic, and tracer data from a fractured-rock aquifer near Mirror Lake, New Hampshire, *Hydrogeol. J.*, *14*(1–2), 1–4, doi:10.1007/s10040-004-0372-y.

Dershowitz, W. S., and H. H. Einstein (1988), Characterizing rock joint geometry with joint system models, in *Rock Mechanics and Rock Engineering*, vol. 21, pp. 21–51, Springer, New York.

Di Federico, V., and S. P. Neuman (1998a), Flow in multiscale log conductivity fields with truncated power variograms, *Water Resour. Res.*, *34*(5), 975–987, doi:10.1029/98WR00220.

Di Federico, V., and S. P. Neuman (1998b), Transport in multiscale log conductivity fields with truncated power variograms, *Water Resour. Res.*, *34*(5), 963–973, doi:10.1029/98WR00221.

Di Federico, V., S. P. Neuman, and D. M. Tartakovsky (1999), Anisotrophy, lacunarity, and upscaled conductivity and its autocovariance in multiscale random fields with truncated power variograms, *Water Resour. Res.*, *35*(10), 2891–2908, doi:10.1029/1999WR900158.

Doughty, C., S. Takeuchi, K. Amano, M. Shimo, and C.-F. Tsang (2005), Application of multirate flowing fluid electric conductivity logging method to well DH-2, Tono Site, Japan, *Water Resour. Res.*, *41*, W10401, doi:10.1029/2004WR003708.

Duguid, J. O., and P. C. Y. Lee (1977), Flow in fractured porous media, *Water Resour. Res.*, *13*(3), 558–566, doi:10.1029/WR013i003p00558.

Dverstorp, B., and J. Andersson (1989), Application of the discrete fracture network concept with field data: Possibilities of model calibration and validation, *Water Resour. Res.*, *25*(3), 540–550, doi:10.1029/WR025i003p00540.

Dverstorp, B., J. Andersson, and W. Nordqvist (1992), Discrete fracture network interpretation of field tracer migration in sparsely fractured rock, *Water Resour. Res.*, *28*(9), 2327–2343, doi:10.1029/92WR01182.

Dykhuizen, R. C. (1990), A new coupling term for dual porosity models, *Water Resour. Res.*, *26*(2), 351–356.

Gerke, H. H., and M. T. van Genuchten (1993a), A dual-porosity model for simulating the preferential movement of water and solutes in structured porous media, *Water Resour. Res.*, *29*(2), 305–319, doi:10.1029/92WR02339.

Gerke, H. H., and M. T. van Genuchten (1993b), Evaluation of a first-order water transfer term for variably saturated dual-porosity models, *Water Resour. Res.*, *29*(4), 1225–1238, doi:10.1029/92WR02467.

Gottlieb, J., and P. Dietrich (1995), Identification of the permeability distribution in soil by hydraulic tomography, *Inverse Problems*, *11*, 353–360, doi:10.1088/0266-5611/11/2/005.

Guimerà, J., L. Vives, and J. Carrera (1995), A discussion of scale effects on hydraulic conductivity at a granitic site (El Berrocal, Spain), *Geophys. Res. Lett.*, *22*(11), 1449–1452, doi:10.1029/95GL01493.

Hao, Y., T.-C. J. Yeh, J. Xiang, W. A. Illman, K. Ando, and K.-C. Hsu (2008), Hydraulic tomography for detecting fracture connectivity, *Ground Water*, *46*(2), 183–192, doi:10.1111/j.1745-6584.2007.00388.x.

Hendricks Franssen, H. J., and J. J. Gómez-Hernández (2002), 3D inverse modeling of groundwater flow at a fractured site using a stochastic continuum model with multiple statistical populations, *Stochastic Environ. Res. Risk Assess.*, *16*(2), 155–174, doi:10.1007/s00477-002-0091-7.

Hsieh, P. A. (1998), Scale effects in fluid flow through fractured geologic media, in *Scale Dependence and Scale Invariance in Hydrology*, edited by G. Sposito, pp. 335–353, Cambridge Univ. Press, Cambridge, U.K.

Hsieh, P. A., S. P. Neuman, G. K. Stiles, and E. S. Simpson (1985), Field determination of the three-dimensional hydraulic conductivity tensor of anisotropic media 2: Methodology and application to fractured rocks, *Water Resour. Res.*, *21*(11), 1667–1676, doi:10.1029/WR021i011p01667.

Hyun, Y., S. P. Neuman, V. V. Vesselinov, W. A. Illman, D. M. Tartakovsky, and V. Di Federico (2002), Theoretical interpretation of a pronounced permeability scale effect in unsaturated fractured tuff, *Water Resour. Res.*, *38*(6), 1092, doi:10.1029/2001WR000658.

Illman, W. A. (1999), Single- and cross-hole pneumatic injection tests in unsaturated fractured tuffs at the Apache Leap Research Site near Superior, Arizona, Ph.D. dissertation, Dep. of Hydrol. and Water Resour., Univ. of Ariz., Tucson.

Illman, W. A. (2004), Analysis of permeability scaling within single boreholes, *Geophys. Res. Lett.*, *31*, L06503, doi:10.1029/2003GL019303.

Illman, W. A. (2005), Type curve analyses of pneumatic single-hole tests in unsaturated fractured tuff: Direct evidence for a porosity-scale effect, *Water Resour. Res.*, *41*, W04018, doi:10.1029/2004WR003703.

Illman, W. A. (2006), Strong field evidence of directional permeability scale effect in fractured rock, *J. Hydrol. Amsterdam*, *319*(1–4), 227–236, doi:10.1016/j.jhydrol.2005.06.032.

Illman, W. A., and D. L. Hughson (2005), Stochastic simulations of steady state unsaturated flow in a three-layer, heterogeneous, dual continuum model of fractured rock, *J. Hydrol. Amsterdam*, *307*(1–4), 17–37, doi:10.1016/j.jhydrol.2004.09.015.

Illman, W. A., and S. P. Neuman (2000), Type-curve interpretation of multirate single-hole pneumatic injection tests in unsaturated fractured rock, *Ground Water*, *38*(6), 899–911, doi:10.1111/j.1745-6584.2000.tb00690.x.

Illman, W. A., and S. P. Neuman (2001), Type-curve interpretation of a cross-hole pneumatic test in unsaturated fractured tuff, *Water Resour. Res.*, *37*(3), 583–604, doi:10.1029/2000WR900273.

Illman, W. A., and S. P. Neuman (2003), Steady-state analyses of cross-hole pneumatic injection tests in unsaturated fractured tuff, *J. Hydrol. Amsterdam*, *281*(1–2), 36–54, doi:10.1016/S0022-1694(03)00199-9.

Illman, W. A., and D. M. Tartakovsky (2005a), Asymptotic analysis of three-dimensional pressure interference tests: Point source solution, *Water Resour. Res.*, *41*, W01002, doi:10.1029/2004WR003431.

Illman, W. A., and D. M. Tartakovsky (2005b), Asymptotic analysis of cross-hole pneumatic injection tests in unsaturated fractured tuff, *Adv. Water Resour.*, *28*(11), 1217–1229, doi:10.1016/j.advwatres.2005.03.011.

Illman, W. A., and D. M. Tartakovsky (2006), Asymptotic analysis of cross-hole hydraulic tests in fractured granite, *Ground Water*, *44*(4), 555–563, doi:10.1111/j.1745-6584.2006.00201.x.

Illman, W. A., D. L. Thompson, V. V. Vesselinov, G. Chen, and S. P. Neuman (1998), Single- and cross-hole pneumatic tests in unsaturated fractured tuffs at the Apache Leap Research Site: Phenomenology, spatial variability, connectivity and scale, *Rep. NUREG/CR-5559*, 186 pp., U.S. Nucl. Regul. Comm., Washington, D.C.

Illman, W. A., X. Liu, and A. J. Craig (2007), Steady-state hydraulic tomography in a laboratory aquifer with deterministic heterogeneity: Multi-method and multiscale validation of hydraulic conductivity tomograms, *J. Hydrol. Amsterdam*, *341*(3–4), 222–234, doi:10.1016/j.jhydrol.2007.05.011.

Illman, W. A., A. J. Craig, and X. Liu (2008), Practical issues in imaging hydraulic conductivity through hydraulic tomography, *Ground Water*, *46*(1), 120–132.

Itoigawa, J. (1980), Geology of the Mizunami district, central Japan (in Japanese), *Monogr. Mizunami Fossil Mus.*, *1*, 1–50.

Knudby, C., and J. Carrera (2005), On the relationship between indicators of geostatistical, flow and transport connectivity, *Adv. Water Resour.*, *28*(4), 405–421, doi:10.1016/j.advwatres.2004.09.001.

Knudby, C., and J. Carrera (2006), On the use of apparent hydraulic diffusivity as an indicator of connectivity, *J. Hydrol. Amsterdam*, *329*(3–4), 377–389, doi:10.1016/j.jhydrol.2006.02.026.

Kumazaki, N., K. Ikeda, J. Goto, K. Mukai, T. Iwatsuki, and R. Furue (2003), Synthesis of the shallow borehole investigations at the MIU construction site, *Tech. Rep. TN7400*, pp. 2003–2005, Jpn. Nucl. Cycle Dev. Inst., Ibaraki, Japan.

Le Borgne, T., O. Bour, F. L. Paillet, and J. P. Caudal (2006), Assessment of preferential flow path connectivity, and hydraulic properties at single-borehole and cross-borehole scales in a fractured aquifer, *J. Hydrol. Amsterdam*, *328*(1–2), 347–359, doi:10.1016/j.jhydrol.2005.12.029.

Li, W., A. Englert, O. A. Cirpka, J. Vanderborght, and H. Vereecken (2007), Two-dimensional characterization of hydraulic heterogeneity by multiple pumping tests, *Water Resour. Res.*, *43*, W04433, doi:10.1029/2006WR005333.

Li, W., A. Englert, O. A. Cirpka, and H. Vereecken (2008), Three-dimensional geostatistical inversion of flowmeter and pumping test data, *Ground Water*, *46*(2), 193–201, doi:10.1111/j.1745-6584.2007.00419.x.

Liu, S., T.-C. J. Yeh, and R. Gardiner (2002), Effectiveness of hydraulic tomography: Sandbox experiments, *Water Resour. Res.*, *38*(4), 1034, doi:10.1029/2001WR000338.

Liu, X., W. A. Illman, A. J. Craig, J. Zhu, and T.-C. J. Yeh (2007), Laboratory sandbox validation of transient hydraulic tomography, *Water Resour. Res.*, *43*, W05404, doi:10.1029/2006WR005144.

Long, J. C. S., J. S. Remer, C. R. Wilson, and P. A. Witherspoon (1982), Porous media equivalents for networks of discontinuous fractures, *Water Resour. Res.*, *18*(3), 645–658, doi:10.1029/WR018i003p00645.

MacQuarrie, K. T. B., and K. U. Mayer (2005), Reactive transport modeling in fractured rock: A state-of-the-science review, *Earth Sci. Rev.*, *72*(3–4), 189–227, doi:10.1016/j.earscirev.2005.07.003.

Marechal, J. C., B. Dewandel, and K. Subrahmanyam (2004), Use of hydraulic tests at different scales to characterize fracture network properties in the weathered-fractured layer of a hard rock aquifer, *Water Resour. Res.*, *40*, W11508, doi:10.1029/2004WR003137.

Martinez-Landa, L., and J. Carrera (2005), An analysis of hydraulic conductivity scale effects in granite (Full-scale Engineered Barrier Experiment (FEBEX), Grimsel, Switzerland), *Water Resour. Res.*, *41*, W03006, doi:10.1029/2004WR003458.

McDermott, C. I., M. Sauter, and R. Liedl (2003), New experimental techniques for pneumatic tomographical determination of the flow and transport parameters of highly fractured porous samples, *J. Hydrol. Amsterdam*, *278*(1–4), 51–63, doi:10.1016/S0022-1694(03)00132-X.

McKenna, S. A., L. C. Meigs, and R. Haggerty (2001), Tracer tests in a fractured dolomite 3. Double-porosity, multiple-rate mass transfer processes in convergent flow tracer tests, *Water Resour. Res.*, *37*(5), 1143–1154, doi:10.1029/2000WR900333.

Menke, W. (1984), The resolving power of cross-borehole tomography, *Geophys. Res. Lett.*, *11*(2), 105–108, doi:10.1029/GL011i002p00105.

Moench, A. F. (1984), Double-porosity models for a fissured groundwater reservoir with fracture skin, *Water Resour. Res.*, *20*(7), 831–846, doi:10.1029/WR020i007p00831.

Molz, F. J., H. Rajaram, and S. Lu (2004), Stochastic fractal-based models of heterogeneity in subsurface hydrology: Origins, applications, limitations, and future research questions, *Rev. Geophys.*, *42*, RG1002, doi:10.1029/2003RG000126.

National Research Council (NRC) (1996), *Rock Fractures and Fluid Flow: Contemporary Understanding and Applications*, Natl. Acad. Press, Washington, D.C.

Neuman, S. P. (1987), Stochastic continuum representation of fractured rock permeability as an alternative to the REV and fracture network concepts, in *Rock Mechanics: Proceedings of the 28th U.S. Symposium*, edited by I. W. Farmer et al., pp. 533–561, A.A. Balkema, Rotterdam, Netherlands.

Neuman, S. P. (2005), Trends, prospects and challenges in quantifying flow and transport through fractured rocks, *Hydrogeol. J.*, *13*(1), 124–147, doi:10.1007/s10040-004-0397-2.

Onoe, H., H. Saegusa, T. Ohyama, and Y. Endo (2007), Stepwise hydrogeological modeling and groundwater flow simulation on site scale (Step4), *Jpn. At. Energy Agency Res.*, *2007–034*, 1–106.

Painter, S., and V. Cvetkovic (2005), Upscaling discrete fracture network simulations: An alternative to continuum transport models, *Water Resour. Res.*, *41*, W02002, doi:10.1029/2004WR003682.

Park, Y.-J., K.-K. Lee, and B. Berkowitz (2001a), Effects of junction transfer characteristics on transport in fracture networks, *Water Resour. Res.*, *37*(4), 909–923, doi:10.1029/2000WR900365.

Park, Y.-J., J.-R. de Dreuzy, K.-K. Lee, and B. Berkowitz (2001b), Transport and intersection mixing in random fracture networks with power law length distributions, *Water Resour. Res.*, *37*(10), 2493–2501, doi:10.1029/2000WR000131.

Park, Y.-J., K.-K. Lee, G. Kosakowski, and B. Berkowitz (2003), Transport behavior in three-dimensional fracture intersections, *Water Resour. Res.*, *39*(8), 1215, doi:10.1029/2002WR001801.

Peters, R., and E. A. Klavetter (1988), A continuum model for water movement in an unsaturated fractured rock mass, *Water Resour. Res.*, *24*(3), 416–430, doi:10.1029/WR024i003p00416.

Power Reactor and Nuclear Fuel Development Corporation (1997), Master plan of regional hydrogeological study (in Japanese), *Tech. Rep. TN702098-001*, Muramatsu, Japan.

Pruess, K., J. S. Y. Wang, and Y. W. Tsang (1990), On thermohydrologic conditions near high-level nuclear waste emplaced in partially saturated fractured tuff: 2. Effective continuum approximation, *Water Resour. Res.*, *26*(6), 1249–1261.

Reimus, P., G. Pohll, T. Mihevc, J. Chapman, M. Haga, B. Lyles, S. Kosinski, R. Niswonger, and P. Sanders (2003), Testing and parameterizing a conceptual model for solute transport in a fractured granite using multiple tracers in a forced gradient test, *Water Resour. Res.*, *39*(12), 1356, doi:10.1029/2002WR001597.

Robinson, T. W. (1939), Earth-tides shown by fluctuations of water-levels in wells in New Mexico and Iowa, *Trans. AGU*, *20*, 656–666.

Salden, W., S. Takeuchi, and Y. Fujita (2005), Use of data from a long-term multi-level groundwater monitoring network to identify the influence of faults, paper presented at 2005 Spring Meeting, Jpn. Groundwater Assoc., Tokyo.

Schwartz, F. W., L. Smith, and A. S. Crowe (1983), A stochastic analysis of macroscopic dispersion in fractured media, *Water Resour. Res.*, *19*(5), 1253–1265, doi:10.1029/WR019i005p01253.

Slough, K. J., E. A. Sudicky, and P. A. Forsyth (1999), Numerical simulation of multiphase flow and phase partitioning in discretely fractured geologic media, *J. Contam. Hydrol.*, *40*(2), 107–136, doi:10.1016/S0169-7722(99)00051-0.

Smith, L., and F. W. Schwartz (1984), An analysis of the influence of fracture geometry on mass transport in fractured media, *Water Resour. Res.*, *20*(9), 1241–1252, doi:10.1029/WR020i009p01241.

Straface, S., T.-C. J. Yeh, J. Zhu, S. Troisi, and C. H. Lee (2007), Sequential aquifer tests at a well field, Montalto Uffugo Scalo, Italy, *Water Resour. Res.*, *43*, W07432, doi:10.1029/2006WR005287.

Tsang, Y. W., C. F. Tsang, F. V. Hale, and B. Dverstorp (1996), Tracer transport in a stochastic continuum model of fractured media, *Water Resour. Res.*, *32*(10), 3077–3092, doi:10.1029/96WR01397.

Vasco, D. W., H. Keers, and K. Karasaki (2000), Estimation of reservoir properties using transient pressure data: An asymptotic approach, *Water Resour. Res.*, *36*(12), 3447–3465, doi:10.1029/2000WR900179.

Vesselinov, V. V., S. P. Neuman, and W. A. Illman (2001a), Three-dimensional numerical inversion of pneumatic cross-hole tests in unsaturated fractured tuff: 1. Methodology and borehole effects, *Water Resour. Res.*, *37*(12), 3001–3018, doi:10.1029/2000WR000133.

Vesselinov, V. V., S. P. Neuman, and W. A. Illman (2001b), Three-dimensional numerical inversion of pneumatic cross-hole tests in unsaturated fractured tuff: 2. Equivalent parameters, high-resolution stochastic imaging and scale effects, *Water Resour. Res.*, *37*(12), 3019–3042, doi:10.1029/2000WR000135.

Wellman, T. P., and E. P. Poeter (2005), Estimating spatially variable representative elementary scales in fractured architecture using hydraulic head observations, *Water Resour. Res.*, *41*, W03001, doi:10.1029/2004WR003287.

Williams, J. H., and F. L. Paillet (2002), Using flowmeter pulse tests to define hydraulic connections in the subsurface: A fractured shale example, *J. Hydrol. Amsterdam*, *265*(1–4), 100–117, doi:10.1016/S0022-1694(02)00092-6.

Wu, Y.-S., W. Zhang, L. Pan, J. Hinds, and G. B. Bodvarsson (2002), Modeling capillary barriers in unsaturated fractured rock, *Water Resour. Res.*, *38*(11), 1253, doi:10.1029/2001WR000852.

Yeh, T.-C. J., and S. Liu (2000), Hydraulic tomography: Development of a new aquifer test method, *Water Resour. Res.*, *36*(8), 2095–2105, doi:10.1029/2000WR900114.

Zhu, J., and T.-C. J. Yeh (2005), Characterization of aquifer heterogeneity using transient hydraulic tomography, *Water Resour. Res.*, *41*, W07028, doi:10.1029/2004WR003790.

Zhu, J., and T.-C. J. Yeh (2006), Analysis of hydraulic tomography using temporal moments of drawdown recovery data, *Water Resour. Res.*, *42*, W02403, doi:10.1029/2005WR004309.

Zimmerman, R. W., G. Chen, T. Hadgu, and G. S. Bodvarsson (1993), A numerical dual-porosity model with semianalytical treatment of fracture/matrix flow, *Water Resour. Res.*, *29*(7), 2127–2137, doi:10.1029/93WR00749.

K. Ando, Civil Engineering Technology Division, Obayashi Corporation, 2-15-2, Konan, Minato-ku, Tokyo, Japan 108-8502.

W. A. Illman, Department of Earth and Environmental Sciences, University of Waterloo, Waterloo, ON N2L 3G1, Canada. (willman@uwaterloo.ca)

X. Liu, Department of Civil and Environmental Engineering, Stanford University, Stanford, CA 94305, USA.

H. Saegusa and S. Takeuchi, Japan Atomic Energy Agency, 1-63, Yamanouchi, Akeyo-cho, Mizunami, Gifu, Japan 509-6132.

T.-C. J. Yeh, Department of Hydrology and Water Resources, University of Arizona, Tucson, AZ 85721, USA.